Rare mutations implicate CGE interneurons as a vulnerable axis of cognitive deficits across psychiatric disorders

Stephanie A. Herrlinger[1, 2]*, Jiayao Wang[3]*, Bovey Y Rao[1,2,4], Jonathan Chang[3], Joseph A. Gogos [1,2,5,6,7]†, Attila Losonczy[1,2]† and Dennis Vitkup[3]†

[1] Department of Neuroscience, Columbia University, New York, NY, United States
[2] Mortimer B. Zuckerman Mind Brain Behavior Institute, Columbia University, New York, NY, United States
[3] Department of Systems Biology and Department Biomedical Informatics, Columbia University, New York, NY, United States
[4] Doctoral Program in Neurobiology and Behavior, Columbia University, New York, NY, United States
[5] Department of Physiology, Columbia University, New York, NY, United States
[6] Department of Psychiatry, Columbia University, New York, NY, United States
[7] Stavros Niarchos Foundation Center for Precision Psychiatry and Mental Health, Columbia University, New York, NY, United States
*These authors contributed equally to this work
† Correspondence should be addressed to JG (jag90@columbia.edu), AL (al2856@columbia.edu) and DV (dv2121@cumc.columbia.edu)

Abstract

Neuropsychiatric disorders such as autism spectrum disorder (ASD) and schizophrenia (SCZ) share genetic risk factors, including genes affected by rare high-penetrance single nucleotide variants (SNVs) and copy number variants (CNVs). ASD and SCZ exhibit both overlapping and distinct clinical phenotypes. Cognitive deficits and intellectual disability—critical predictors of long-term outcomes—are common to both conditions. To investigate shared and disorder-specific neurobiological impact of highly penetrant rare mutations in ASD and SCZ, we analyzed human single-nucleus whole-brain sequencing data to identify strongly affected brain cell types. Our analysis revealed caudal ganglionic eminence (CGE)-derived GABAergic interneurons as a key nexus for cognitive deficits across these disorders. Notably, genes within 22q11.2 deletions, known to confer a high risk for SCZ, ASD, and cognitive impairment, showed a strong expression bias toward vasoactive intestinal peptide-expressing cells (VIP+) among CGE subtypes. To explore perturbations of VIP+ GABAergic interneurons in the 22q11.2 deletion syndrome *in vivo*, we examined their activity in the *Df(16)A*$^{+/-}$ mouse model during a spatial navigation task and observed reduced activity along with altered responses to random rewards. At the population level, VIP+ interneurons exhibited impaired spatial encoding and diminished subtype-specific activity suggesting deficient disinhibition in CA1 microcircuits in the hippocampus, a region essential for learning and memory. Overall, these results demonstrate the crucial role of CGE-derived interneurons in mediating cognitive processes that are disrupted across a range of psychiatric and neurodevelopmental disorders.

Introduction

Psychiatric disorders exhibit distinct clinical symptoms, yet frequently share genetic risk factors and underlying cellular and molecular mechanisms[1–6]. For example, schizophrenia (SCZ) is characterized by psychosis, including hallucinations and delusions, as well as cognitive control impairments leading to disorganization, impulsivity, and difficulties with working memory[7–11]. In contrast, autism spectrum disorder (ASD) is characterized by restricted interests, difficulties with social communication, and cognitive rigidity along with repetitive behaviors[8,12]. Several copy number variations (CNVs), such as the 22q11.2 deletion, have been implicated in both SCZ and ASD, as well as in other psychiatric disorders[13,14]. Among their diverse symptoms, cognitive impairments and intellectual disability (ID) are frequently comorbid with neuropsychiatric phenotypes[15] and are especially pronounced in cases with high genetic risk[15–18]. Cognitive deficits in psychiatric disorders are particularly debilitating, and span a broad range of functions, including memory, attention, reasoning, decision-making and social cognition[19]. The severity of these deficits is a strong predictor of patients' long-term health outcomes and overall well-being[20–22].

Despite advances in the genetics of disorders such as ASD and SCZ[1,2,23], therapeutic progress in treating their cognitive symptoms remains limited, largely due to gaps in understanding the neurobiological mechanisms through which genetic risk factors impact cognition. To better understand the relationships between genetics and psychiatric phenotypes, researchers are increasingly integrating genetic analyses with single-cell and single-nucleus sequencing data to identify cell types affected across psychiatric disorders[24–26]. Animal models, particularly mouse models that replicate rare, high-risk genetic insults, play a critical role in this integrative approach. The evolutionary conservation of brain regions, cell types, and core biological processes between mice and humans[27–30] facilitates the detailed examination of genetic risk factors at both the cellular and circuit levels[31–36].

In this study, we investigated the neurobiological impact of rare, highly penetrant mutations in ASD, SCZ, and 22q11.2 deletion syndrome across diverse brain cell types, using recently released human single-nucleus whole-brain RNA sequencing data[37] (Figure 1, left). Our analyses revealed distinct disorder-specific mutation biases affecting different cell types, with caudal ganglionic eminence (CGE)-derived interneurons consistently implicated across genetic insults associated with cognitive dysfunction, including ASD with intellectual disability, SCZ, and Developmental Disorders and Intellectual Disability (DD/ID) (Figure 1, middle). Furthermore, our analysis of genes within the 22q11.2 deletion revealed that VIP+ CGE-derived interneurons were strongly affected in this condition. Using *in vivo* two-photon calcium imaging of VIP+ GABAergic interneuron activity in a mouse model of 22q11.2 deletion, we observed specific alterations in interneuron-selective interneuron (ISI) cell types, which primarily inhibit other interneurons (Figure 1, right). These findings implicate ISI dysfunction in circuit-level abnormalities contributing to cognitive and behavioral phenotypes of this syndrome, and likely many other psychiatric conditions.

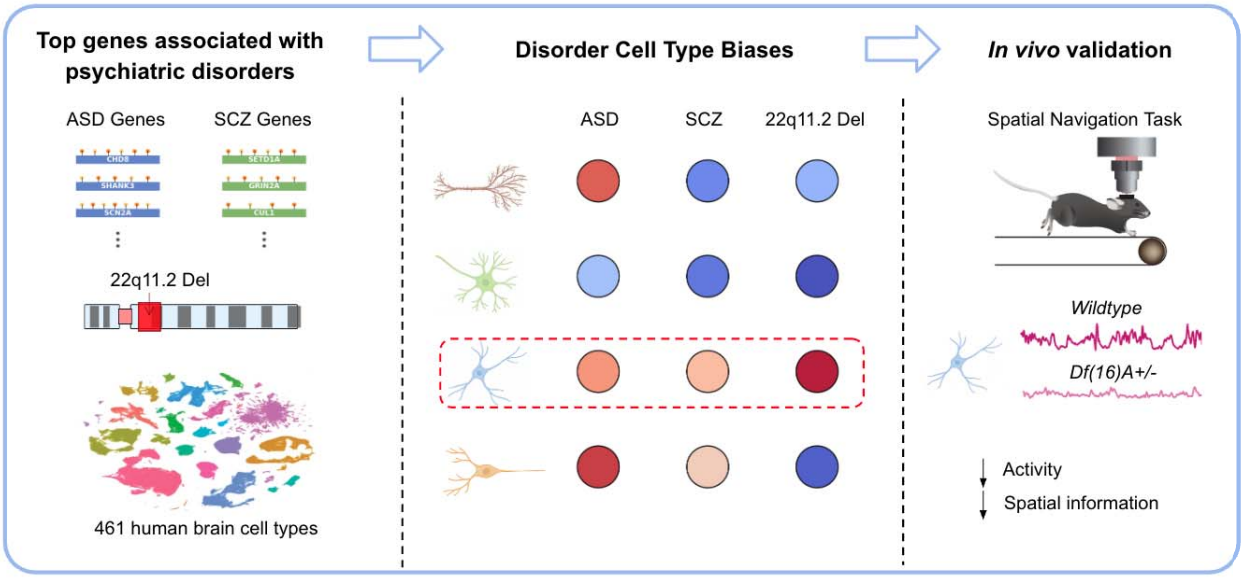

Figure 1. Overview of study. Left: Integration of genetic and single-cell transcriptomic data was used to identify cell type-specific disorder biases. Genes implicated in ASD and SCZ[1,2] and genes in the 22q11.2 deletion were used to calculate cell type mutation biases based on human brain snRNA-seq data from 461 cell types[37]. **Middle:** Disorder cell type bias analysis revealed shared cell type risk patterns between distinct disorders with overlapping cognitive phenotypes. **Right:** Experimental analysis of the 22q11.2 deletion mouse model was used to identify cell type specific deficits *in vivo* using 2-photon calcium imaging to capture neuronal activity during a spatial navigation task.

Results

Identifying disorder-specific cell type mutation biases by leveraging genetic and single-nucleus expression data

Individually, highly penetrant rare mutations typically have substantially greater functional impacts on psychiatric phenotypes compared to common variants[1,38]. The availability of well-characterized rare variant datasets from ASD and SCZ cohorts has allowed us to perform direct cross-disorder comparisons. For ASD, we utilized a recent meta-analysis performed by the SPARK consortium[2], which comprised *de novo* mutations from 42,607 ASD probands. This analysis identified 61 genes with exome-wide significance by de novo mutations. For schizophrenia, we used a case-control study involving 24,248 schizophrenia patients and 97,322 control individuals from the SCHEMA consortium[1]. In our analysis, we selected the top 61 SCZ genes based on genetic association strength to match the number of considered ASD-associated genes.

A significant fraction of probands in the ASD cohort exhibit low IQs (IQ ≤ 70, which we refer to as “ASD with ID”)[39,40] (Figure S1). To facilitate a more appropriate comparison with SCZ, where the average premorbid IQ is approximately 94[41,42], we selected higher IQ (IQ >70) ASD cases from the SPARK cohort (hereafter referred to as “ASD”, with an average IQ approximately 95).

Notably, individuals with SCZ who carry rare mutations have IQ scores that are only marginally lower than those in the broader schizophrenia population[43]. Furthermore, genes implicated in higher-IQ ASD also share more similar developmental expression profiles with SCZ genes compared to those associated with lower-IQ ASD (Figure S2). It is important to emphasize that even though SCZ and ASD cases have comparable overall IQs, the nature of cognitive dysfunction in these conditions is often distinct. While SCZ is usually characterized by broad deficits across multiple cognitive domains, such as working memory and executive function[44,45], high-functioning ASD cases tend to show more selective, domain-specific cognitive impairments, particularly in social cognition and communication[46,47].

To identify the brain cell types most impacted by rare coding mutations in ASD and SCZ, we used a recent single-nucleus sequencing dataset collected from the entire human brain[37]. This dataset encompassed approximately 105 anatomical locations dissected from three different donors across the forebrain, midbrain, and hindbrain, with 3,369,219 individual nuclei classified into 31 cell type superclusters, representing broad categories of major brain cell classes, and 461 cell type clusters, which provide finer-grained subdivisions based on robust transcriptomic similarity. (Figure 1). To evaluate the impact of mutations on brain cell types in ASD and SCZ, we calculated mutation biases across brain cell types by integrating gene expression with disorder-specific mutation burden (Figure S3, see Methods). We first computed a cell type specificity score for each gene, quantifying how selectively a gene is expressed in a given cell type relative to others[26]. To that end, we first quantified gene expression levels using transcripts per million (TPM) for each cell type, and then used TPM values to compute specificity scores capturing the enrichment of each gene's expression in different cell types. Next, to assess how strongly each cell type is implicated in the disorders, we integrated the expression specificity scores with each gene's mutation burden, using *de novo* mutation counts for ASD and effective case mutation counts for SCZ. The resulting cell-type mutation bias captured how selectively disease genes are expressed in each cell type, weighted by their mutational burden in diagnosed patient cohorts. To evaluate statistical significance of our mutation biases, we compared the observed bias for each cell type cluster to a null distribution generated from 10,000 random gene sets matched in size to the disorder-specific gene set, with the original mutation weights randomly reassigned to these sets. Empirical P-values were calculated from these simulations and corrected for multiple testing across 461 clusters. These mutation bias results were robust across a range of gene set sizes (Figure S4).

Shared cell type mutation biases in ASD and SCZ

The cell types that showed strong mutation biases in ASD included amygdala excitatory neurons, medium spiny neurons, hippocampal dentate gyrus neurons, and deep-layer intratelencephalic (IT) neurons (Figure S5A). The same cell type superclusters also showed strong mutational impacts in ASD with ID, with additional significant cell types including excitatory neurons from the cortex and hippocampus, as well as cortical interneurons (Figure S5B). For SCZ, cells with strong mutational impacts included several cell types implicated in recent GWAS studies of SCZ[25,26]. Specifically, MGE interneurons were the most strongly impacted cell type, with eccentric medium spiny neurons, Lamp5-LHX6 and Chandelier neurons,

CGE interneurons, upper- and deep-layer IT neurons, and midbrain-derived inhibitory neurons also strongly affected. Other significantly impacted cell types included amygdala excitatory neurons, mammillary body neurons, and hippocampal dentate gyrus and CA1-3 neurons (Figure S5C).

Several cell type superclusters were strongly impacted by mutations in both ASD and SCZ, including excitatory neurons in the amygdala and hippocampus, as well as cortical excitatory neurons (such as upper-layer IT, deep-layer IT, deep-layer corticothalamic, and layer 6b neurons) (Figure 2C, Figure S5A-S5C, Figure S7A-S7D). These findings are consistent with several previous studies demonstrating frequent perturbations of these neurons across brain disorders. For example, amygdala neurons and their cortical and hippocampal projections have been implicated in a broad range of behavioral disturbances in SCZ and ASD, including deficits in emotion, motivation, and social interactions[48,49]. Moreover, the hippocampus is known to play a key role in social and cognitive deficits in ASD[50], as well as in learning deficits and positive symptoms associated with SCZ[51,52]. Deep-layer IT neurons, which are central to sensory processing, decision-making, and learning, are also known to be strongly affected in both disorders[53]. Overall, these shared neuronal disruptions may underlie the overlapping dysfunction of brain circuits mediating psychiatric phenotypes[54].

Our analysis revealed a strong correlation between ASD and SCZ mutation biases across neuronal cell type clusters (Figure 2A), with cell types showing strong mutation biases in ASD usually also showing strong mutation biases in SCZ (Spearman's correlation = 0.68, $P < 10^{-10}$). Notably, the correlation between cell type biases was not due to the overlap between ASD and SCZ in implicated genes (Spearman correlation = 0.64, $P < 10^{-10}$, after removing three overlapping genes). To understand what influences the shared cell type biases between the disorders, we investigated the role of genes with strong constraint against loss-of-function mutations, as constrained genes often have a substantial mutation burden in psychiatric disorders[1,2,39,55,56]. When we progressively removed genes from the considered disorder-specific sets (one gene at a time, ranked by their loss-of-function constraint LOEUF score[57], see Methods), the correlation between ASD and SCZ substantially decreased after the removal of approximately 15 genes (Figure 2B, red); in contrast, removing the least constrained genes preserved the substantial correlation between mutation biases (Figure 2B, blue). We next asked whether gene expression levels across cells might also contribute to the shared correlation of mutation biases between ASD and SCZ, as both disorders involve genes highly expressed in the brain[3,58]. Interestingly, in contrast to gene mutation constraint, removing highly expressed genes had little impact on the cell type bias correlation (Figure S6). These findings suggest that highly constrained genes harboring disease-associated mutations tend to be preferentially expressed in cell types that are primarily targeted by mutations in both disorders.

Distinct cell type mutation biases in ASD and SCZ

Given the overall similarity in cell type mutation biases between ASD and SCZ, we next sought to identify cell types preferentially affected in one disorder relative to the other. To that end, we

calculated, for each cell type, the differential mutation bias between ASD and SCZ across cell type clusters within each cell type supercluster. This differential bias measure quantifies how strongly each cell type supercluster is preferentially affected in one disorder compared to the other, potentially underlying the unique behavioral phenotypes associated with each disorder. We observed that mutations in ASD and SCZ are differentially biased toward several specific neuron types (Figure 2C). Specifically, medium spiny neurons (MSNs) showed substantially stronger mutation biases in ASD compared to SCZ (Figure 2D). This agrees with previous findings implicating MSNs in ASD in computational[58] and experimental studies[59,60]. In contrast, GABAergic interneurons, including MGE-derived, CGE-derived, and Lamp5-LHX6/Chandelier interneurons showed the strongest differential biases towards SCZ compared to ASD (Figure 2C, 2E and 2F), which is consistent with previous studies implicating interneurons in SCZ[25,26,61,62]. As mentioned above, cognitive impairments are widespread in schizophrenia, while cognitive symptoms in high-functioning ASD are often more localized and specific[44–47]. Considering this, we investigated which neuron types were more affected in ASD probands with ID compared to ASD probands without ID. This analysis showed that all three interneuron superclusters had substantially stronger biases toward ASD with ID compared to high-functioning ASD, with CGE interneurons showing the strongest differential bias (Figure S7E, Figure 2G). Overall, these results suggest a potential role of interneurons, particularly CGE-derived interneurons, in cognitive dysfunctions observed in both ASD with ID and SCZ.

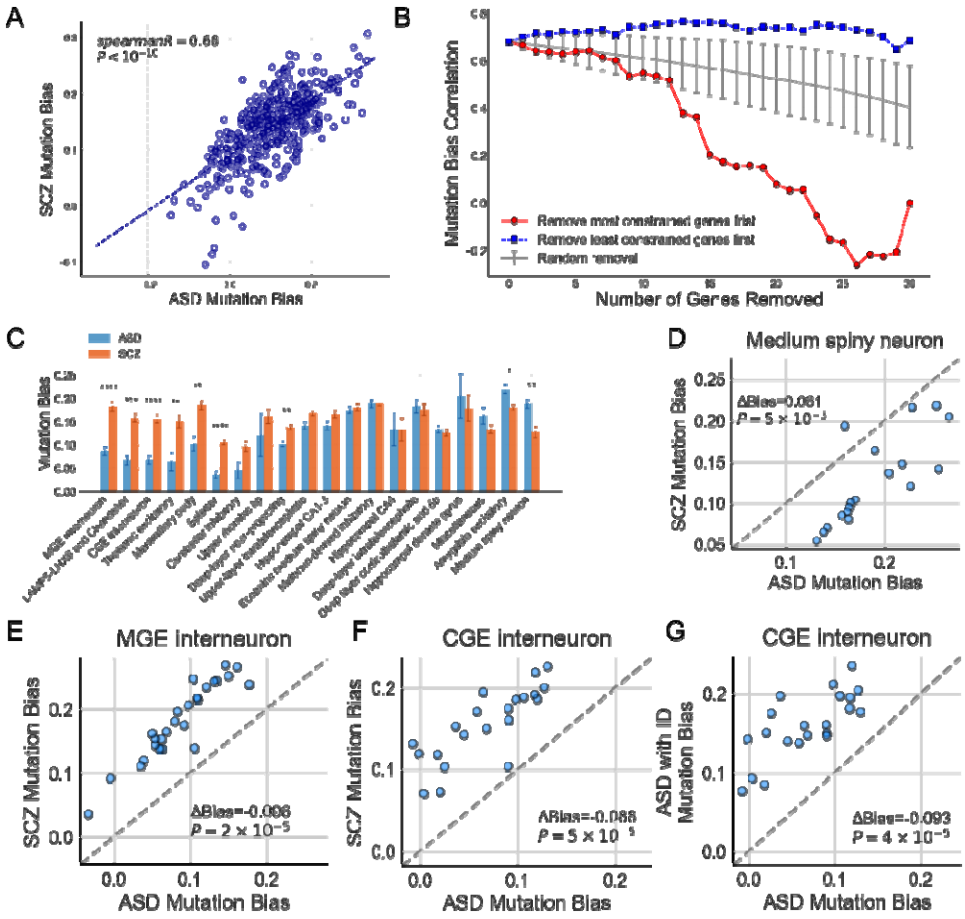

Figure 2. ASD and SCZ Mutation bias towards different brain cell types. **A**. The correlation of mutation biases between ASD and SCZ across all neuronal cell types (Spearman R = 0.68, P < 10^{-10}). Each dot represents a neuron cell type cluster. **B**. Spearman correlation of cell type bias between ASD and SCZ genes, assessed by sequential gene removal. Genes were removed one at a time from each disorder's gene set in parallel, either starting from the most constrained (blue) or least constrained (red) based on LOEUF score. At each step, ASD–SCZ bias correlations were recomputed using mutation biases obtained from the remaining genes. The gray line shows the average correlation for random gene removals, with error bars indicating ±1 standard deviation. **C**. Bar plot comparing mutation biases across cell type superclusters between ASD (blue) and SCZ (orange). All neuronal cell types at supercluster level are displayed and sorted by average differential bias between ASD and SCZ. Error bars represent standard error across cluster biases from corresponding supercluster. Asterisks indicate significance level between groups *: P < 0.05. **: P < 0.01. ***: P < 0.001, ****: P < 0.0001, Mann-Whitney U test with FDR correction. **D-G.** Detailed comparison of mutation biases in specific neuron superclusters, each point representing a cell type cluster from the corresponding supercluster, P-values were calculated based on Mann–Whitney U test with FDR correction. **(D)** Medium spiny neurons show stronger bias in ASD. **(E)** MGE interneurons exhibit stronger bias in SCZ, **(F)** CGE interneurons display bias toward SCZ and **(G)** CGE interneurons show stronger bias when comparing ASD with ID to ASD.

CGE interneurons are strongly affected in multiple psychiatric phenotypes with cognitive impairments

To further explore the involvement of CGE interneurons in cognitive function, we analyzed several additional cohorts with related phenotypes (Figure 3A, see Methods). Consistent with our observation of stronger CGE interneuron bias in SCZ and ASD with ID, we also observed a strong bias toward CGE interneurons (Figure 3A; Figure S7H) in the developmental disorders and intellectual disability (DD/ID) cohort[56], which is characterized by severe cognitive impairments. Furthermore, we analyzed rare protein-coding variants available in the UK Biobank associated with cognitive functions, including verbal-numerical reasoning (VNR), reaction time (RT), and educational attainment (EDU)[63]. We found that genes negatively associated with VNR (VNR-), i.e., genes with mutations leading to worse VNR performance, an assessment of fluid intelligence and best proxy to general intelligence among the traits[64] (see Methods), exhibited a pronounced bias toward CGE interneurons compared to genes positively associated with VNR (VNR+, Figure 3A and S7G). When we compare bias contrast of all three major interneuron groups, we find in contrast to CGE interneurons, MGE and Lamp5-LHX6/Chandelier interneurons showed relatively weaker mutation biases across the additional cohorts we examined (Figure 3B, Figure S8). The consistently strong CGE interneuron mutation bias across different cohorts suggests that these neurons play a key role in cognitive processes.

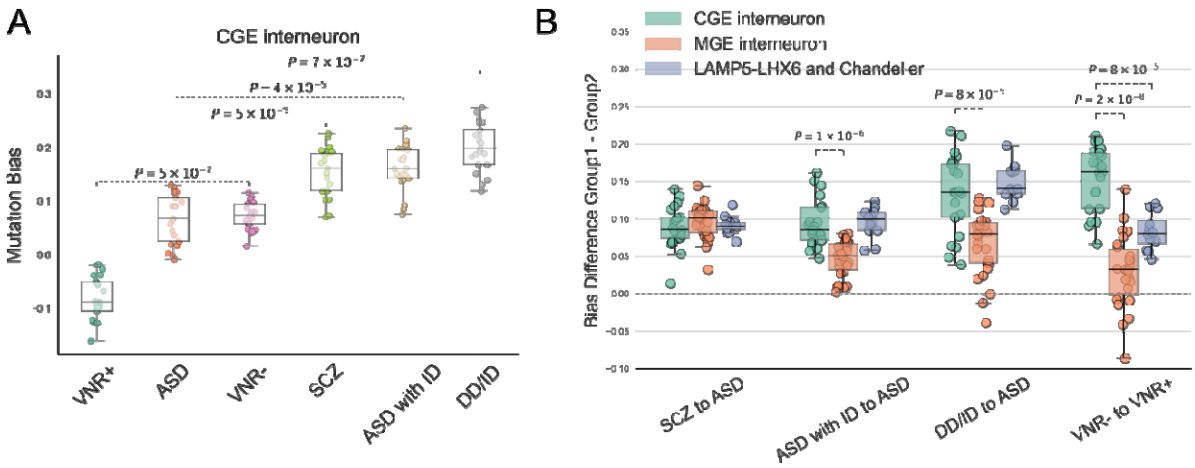

Figure 3. CGE interneurons are impacted in multiple cohorts with cognitive abnormalities. A. CGE interneuron mutation biases across different cohorts shows stronger bias in disorders with cognitive deficits. Each dot represents a CGE interneuron subtype. Comparison includes ASD (without ID), verbal-numerical reasoning negative and positively associated genes (VNR- and VNR+), schizophrenia (SCZ), ASD with ID, and developmental disorders/intellectual disability (DD/ID). P-values indicate the significance of differences in CGE interneuron mutation biases between groups (e.g., SCZ, DD/ID and ASD with ID vs. ASD, VNR– vs. VNR+) and were calculated using the Mann–Whitney U test with FDR correction. **B.** Pairwise mutation bias differences between disorders across 3 major interneuron superclusters. For each disorder pair (Group1 – Group2), the y-axis shows the difference in mutation bias per cell type cluster. Each dot represents one cluster from the three interneuron superclusters (CGE, MGE, LAMP5-LHX6/Chandelier). Colored boxplots indicate the supercluster of origin. Statistical comparisons were conducted between CGE clusters and each of the other two superclusters (MGE, LAMP5-LHX6/Chandelier) using the Mann–Whitney U test. Significant (0.05/8 comparisons) differences are annotated with the corresponding p-values.

VIP+ interneurons are strongly affected by genes in the 22q11.2 deletion

Copy number variants (CNVs) consistently stand out as highly penetrant genetic risk factors for SCZ and ASD[15,36,65,66]. 22q11.2 deletion syndrome is a neurodevelopmental disorder characterized by a significantly elevated risk of schizophrenia in adulthood, along with comorbidities such as ASD and intellectual disability[14,67]. Cognitive impairment is a key feature of 22q11.2 deletion syndrome, with nearly half of affected individuals displaying an IQ below 70[68,69]. Similar to most disease-associated CNVs, the full range of phenotypic symptoms results from the synergistic effects of multiple genes within the 22q11.2 deletion[14]. Given the significant SCZ risk and cognitive disability phenotypes associated with the 22q11.2 deletion, we next investigated the bias toward CGE and other interneurons among the deletion genes. The 22q11.2 deletions occur in two main forms: a 3 Mb deletion (containing 46 genes) and a smaller 1.5 Mb deletion (containing 28 genes). Analysis of cell type biases for genes in the 3 Mb deletion (Figure S9) revealed a substantial bias toward CGE-derived interneurons compared to other major interneuron types (Figure 4A). Notably, among CGE interneurons, VIP+ cell types exhibited significantly stronger biases compared to VIP- CGE cell types (Figure 4B). This pattern remained consistent and significant when examining genes within the 1.5 Mb deletion, which corresponds to the 16qA13 deletion in mouse (Figure 4B). The selective impact on VIP+ interneurons compared to other CGE interneuron types suggests a particularly important role in mediating the severe cognitive and behavioral phenotypes associated with 22q11.2 deletion

syndrome. CGE-derived VIP+ interneurons modulate neural circuits by reducing inhibition and enhancing excitatory activity[70,71], an essential mechanism for cognitive functions such as perception, attention, learning and memory[72]. They achieve this by suppressing Sst+, Cck+, and possibly Pvalb+ GABAergic interneurons[73,74], thereby indirectly amplifying pyramidal neuron activity. Moreover, VIP+ interneurons interact with cholinergic, serotonergic, and dopaminergic systems[74–79] to maintain the excitation-inhibition balance critical for network stability and effective cognitive processing[72].

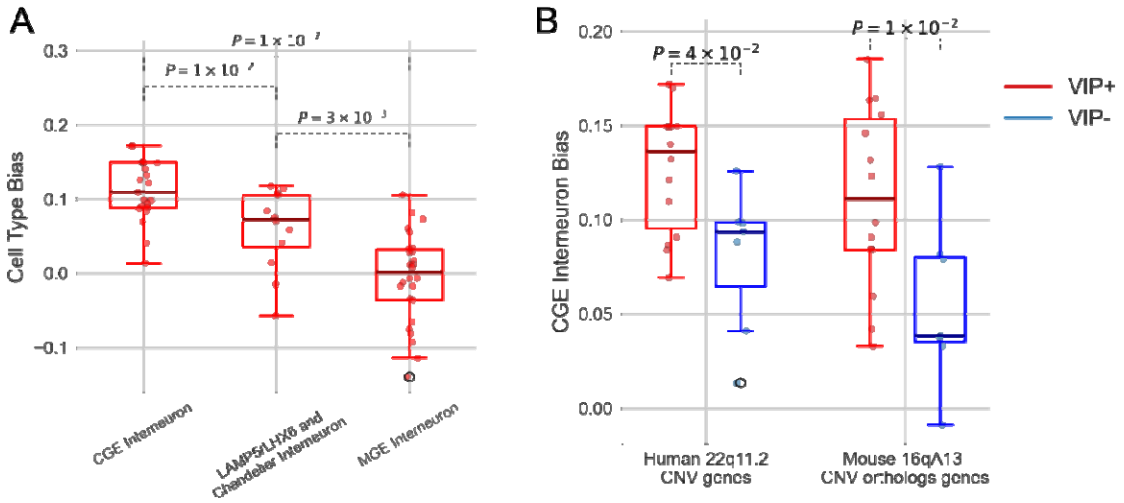

Figure 4. VIP+ CGE interneurons are preferentially affected by 22q11.2 deletion genes. (A) Boxplot showing expression biases for three major interneuron types (CGE interneurons, Lamp5/LHX6 and Chandelier cells, and MGE interneurons) in the 22q11.2 deletion region. CGE interneurons exhibit the strongest bias compared to other interneuron populations (P-values shown for pairwise comparisons, Mann-Whitney U-test). **(B)** The CGE interneuron cell type bias across different 22q11.2 gene sets, including complete deletion genes (3MB deletion, 46 genes) and 28 genes included in 1.5MB deletion which is equivalent to mouse 16qA13 deletion. VIP+ CGE types shown in red and VIP- CGE types shown in blue. Difference between VIP+ and VIP- bias is significant for all 22q11.2 genes and 1.5MB deletion genes (P=0.04 and 0.01, respectively, Mann-Whitney U-test.)

Altered VIP+ interneuron activity and population specificity in a mouse model of 22q11.2 deletion syndrome

Having identified a robust genetic association between mutation biases toward CGE interneurons and cognitive phenotypes across multiple genetic disorders, and a prominent bias of VIP+ cell types compared to other interneurons in 22q11.2 deletion syndrome, we next experimentally investigated whether and how this bias is reflected in the altered function of these interneurons within hippocampal circuitry. To this end, we used the *Df(16)A*$^{+/-}$ mouse model, which faithfully recapitulates the human 1.5 Mb 22q11.2 deletion[13,33,35,80]. This model, known for deficits in working and episodic memory, synaptic plasticity, and cortical and hippocampal development, has proven invaluable for uncovering novel biological pathways relevant to cognitive dysfunction and psychiatric disorders[14,35,36,67,80–83]. We therefore examined the physiological impact of the 22q11.2 deletion on specific CGE/VIP+ cell types, thus

advancing our understanding of the cellular mechanisms by which CGE-derived VIP+ interneurons mediate cognitive processes are disrupted in 22q11.2 deletion syndrome.

To examine VIP+ interneuron activity *in vivo*, we crossed *Df(16)A*$^{+/-}$ mice with VIP-Cre mice and locally injected an adenovirus carrying a floxed GCaMP8m or GCaMP7f calcium indicator into the CA1 region to selectively express GCaMP in VIP+ interneurons (Figure S10A). Using two-photon three-dimensional acousto-optic deflector (3D-AOD)[84–86] microscopy, we then recorded VIP+ interneuron activity in a 3D volume within the dorsal hippocampal CA1 region (Figure S10B-S10D). Tissue registration and *post-hoc* immunohistochemistry[32,84,87] (see Methods, Figure S10E, S10F) allowed us to identify four major VIP+ interneuron subtypes: interneuron-selective interneurons type 2 (ISI2), interneuron-selective interneurons type 3 (ISI3), VIP+ cholecystokinin basket cells (CCKBCs), and a group of VIP-expressing cells, referred to as "VIP+ only" (VIPo) cells, that were immunonegative for all other tested markers[70,88,89]. The distribution of these subtypes across hippocampal layers did not significantly differ between wild type and *Df(16)A*$^{+/-}$ mice (Figures S10G and S10H), and comparable numbers of each interneuron subtype were recorded from both wild type and mutant genotypes (Figures S10I). Thus, our analysis did not find evidence that the 22q11.2 deletion affects the number or proportion of VIP+ interneuron subtypes in the hippocampal CA1 region.

As previously established, global interneuron activity is strongly driven by ambulatory state[90–93], and in treadmill-based experiments we consistently observed that locomotion is the greatest predictor of global interneuron activity[32,84,94]. To investigate locomotion-related activity of hippocampal VIP+ interneurons, mice were next trained to run on a head-fixed, cue-rich 2-meter treadmill for randomly distributed water rewards while undergoing calcium imaging (Figure 5A)[32,84,87]. Behavioral metrics, including laps run, licking, and region occupancy on the belt during the 10-minute trials, were similar across genotypes (Figures S10J-S10M). Expected locomotion-related activity patterns were preserved across genotypes, with ISI3, ISI2, and VIPo subtypes positively correlated with movement, and VIP+ CCKBCs anticorrelated (Figure 5B)[84,95]. However, in *Df(16)A*$^{+/-}$ mice, ISI3 and ISI2 cell activity exhibited a significantly reduced correlation with locomotion (Figure 5C), and ISI3, ISI2, and VIPo interneurons showed visibly reduced calcium transient amplitudes (Figure 5B). Due to the spike-like activity of ISI3, ISI2, and VIPo cells we were able to perform a transient waveform analysis (see Methods[96]). This analysis confirmed reduced amplitudes in ISI3, ISI2, and VIPo cells (Figures 5D-J), while VIPo cell transients uniquely occurred at a higher frequency (Figure 5J). Reward responses, accessed by Peri-event Time Averages (PETA, see Methods), exhibited genotype-dependent differences, including reduced VIPo response amplitudes and enhanced ISI2 and ISI3 response amplitudes (Figures 5K, 5L), suggesting that ISIs in mutant mice exhibit heightened sensitivity to random salient features[94]. Overall, these results show that VIP+ interneurons in the hippocampal CA1 region exhibit reduced *in vivo* activity dynamics in the 22q11.2 deletion model and that reward responses are significantly altered among specific VIP+ subtypes, demonstrating physiological consequences of the genetic perturbation predicted by our computational analysis.

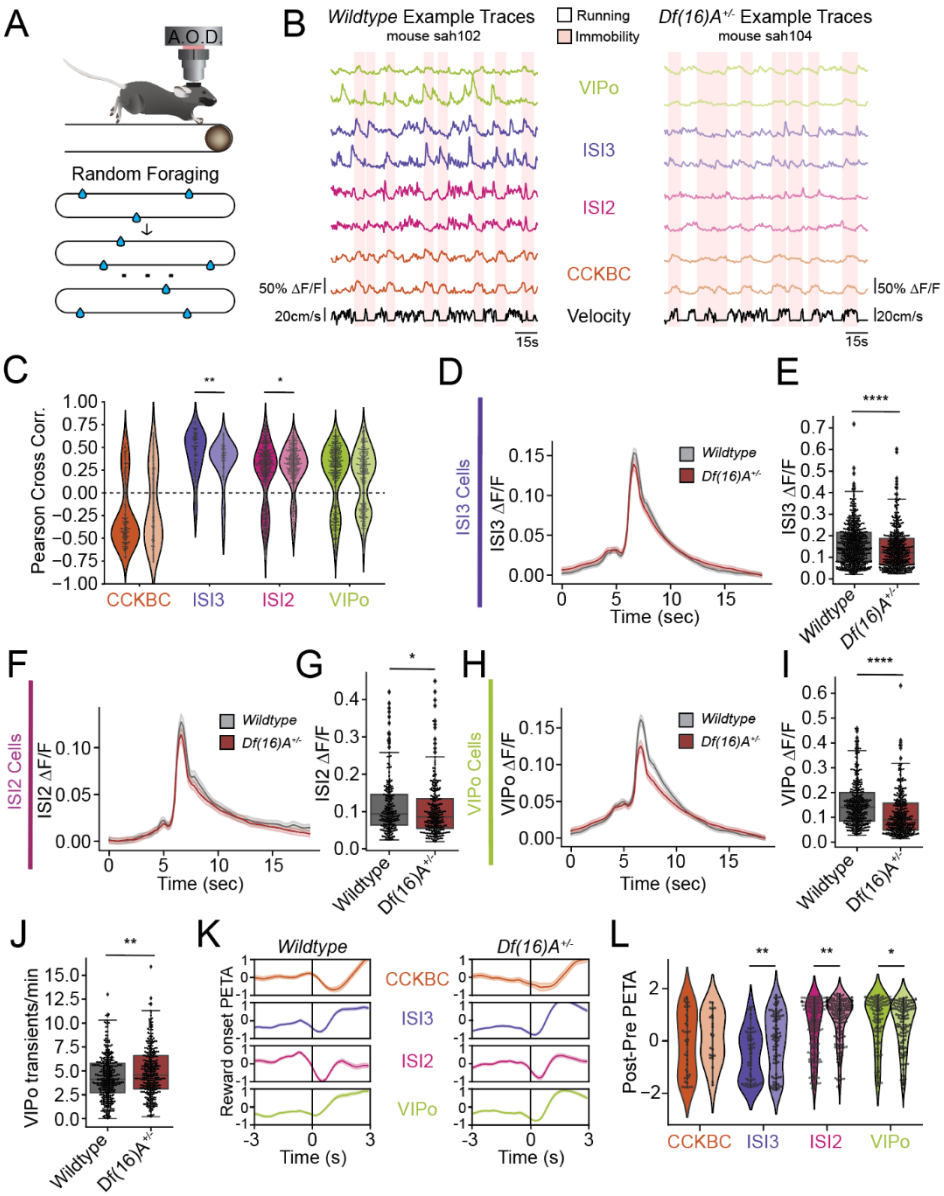

Figure 5: Baseline changes in VIP+ cell type calcium dynamics in mutant mice. A. Imaging and behavior schematic: mice are trained to run on a cue-rich belt to expect random water rewards to be deposited across the belt (bottom) while head-fixed and imaged with 2-photon 3D-AOD microscopy (top). **B.** Example traces from all four VIP+ cell types detected in a single session from a Wildtype littermate (left) and a *Df(16)A*$^{+/-}$ (right) mouse. **C.** Pearson correlation coefficients of mouse velocity against average subtype calcium activity. **D.** Waveform comparison of average detected calcium transient from wildtype littermates (black) and *Df(16)A*$^{+/-}$ (brown) ISI3 cells. **E.** Average amplitude of detected ISI3 waveforms compared between genotypes. **F.** Waveform comparison of average detected calcium transients from wildtype littermates (black) and Df(16)A$^{+/-}$ (brown) ISI2 cells. **G.** Average amplitude of detected ISI2 waveforms compared between genotypes. **H.** Waveform comparison of average detected calcium transients from wildtype littermates (black) and *Df(16)A*$^{+/-}$ (brown) VIPo cells. **I.** Average amplitude of detected VIPo waveforms compared between genotypes. **J.** Number of transients from VIPo cells per cell between genotypes. **K.** Averaged z-scored reward-onset peri-event time averages (PETAs) between -1.0 and 1.0 z-scores by cell type across all cells within cell type during the Random Foraging task for 3 seconds pre- and 3 seconds post-event. **L.** Post - Pre PETA responses per cell type before and after reward onset comparing the 3 seconds pre- to 3 seconds post-event. *CCKBC:* VIP+ and cholecystokinin + basket cell; *ISI3:* Interneuron-selective interneuron type 3; *ISI2:*

Interneuron-selective interneuron type 2; *VIPo*: VIP+/Cal-/M2R-/CCK- cells in layer oriens or layer pyramidale. *: P < 0.05. **: P < 0.01. ****: P < 0.0001. See Table S1 for detailed statistics.

Hippocampal place cells, a subset of pyramidal neurons, are active in specific environmental locations and provide cellular substrates for episodic memory and goal-directed spatial learning[97,98]. In *Df(16)A*$^{+/-}$ mice, our previous study revealed significant impairments in learning performance when both contextual cues and reward locations were altered during a spatial navigation task[82]. These learning deficits were associated with reduced long-term stability of place fields, impaired context-related remapping and plasticity, and a lack of reward-related reorganization. Further investigation showed that parvalbumin- and somatostatin-expressing GABAergic interneurons, which are directly inhibited by VIP+ cell activity, displayed diminished place fields and heightened reward-related activity, likely contributing to the observed place cell deficits[32]. Changes in the activity dynamics of VIP+ cells in dorsal CA1 may also reflect altered spatial information encoding by these cells. To explore this, we next evaluated how well mouse position could be decoded based on VIP+ subtype activity during random foraging (Figure 5A) by training a support vector machine using all recorded interneuron activity (Figure 6A). Decoding error did not differ between genotypes when the total number of imaged cells per session was not normalized. However, when controlling for the number of cells tested (Figure 6B) or the number of laps run per session (Figure 6C), decoding error was significantly higher in *Df(16)A*$^{+/-}$ mice, indicating that individual mutant cells carry less spatial information than cells in wild type mice. Furthermore, analysis of place preference in VIP+ cell activity revealed that fewer VIP+ cells in *Df(16)A*$^{+/-}$ mice exhibited significant place fields, with a reduced proportion displaying at least one place field (Figure 6D). These findings demonstrate that VIP+ interneurons in the 22q11.2 deletion model exhibit markedly impaired spatial encoding within the CA1 microcircuit.

Local brain circuits balance coordinated and unique activity depending on input properties, connectivity, and brain state. Taking advantage of our simultaneous recordings across multiple VIP+ subtypes in our experiments, we computed pairwise Pearson's correlation coefficients between calcium activity traces within and between different VIP+ interneuron subtypes (see Methods). We found that VIP+ cells in *Df(16)A*$^{+/-}$ mice exhibited unusually high correlations between subtypes during random foraging. This suggests a loss of subtype-specific heterogeneity of *in vivo* activity dynamics, particularly among disinhibitory VIP+ subtypes, indicating a potential microcircuit-level disruption and impaired fine-scale coordination between VIP+ interneuron subtypes (Figures 6E and 6F). These findings reveal that VIP+ interneurons in the CA1 region of *Df(16)A*$^{+/-}$ mice exhibit impaired spatial encoding — reflected in increased decoding errors and reduced place preference — and that this disruption is also accompanied by a loss of subtype-specific heterogeneity, evident from unusually high inter-subtype correlations during the foraging task. These physiological consequences align with our computational analyses and illuminate how perturbations in specific subtypes of VIP+ interneurons can disrupt network dynamics and information processing important for cognition.

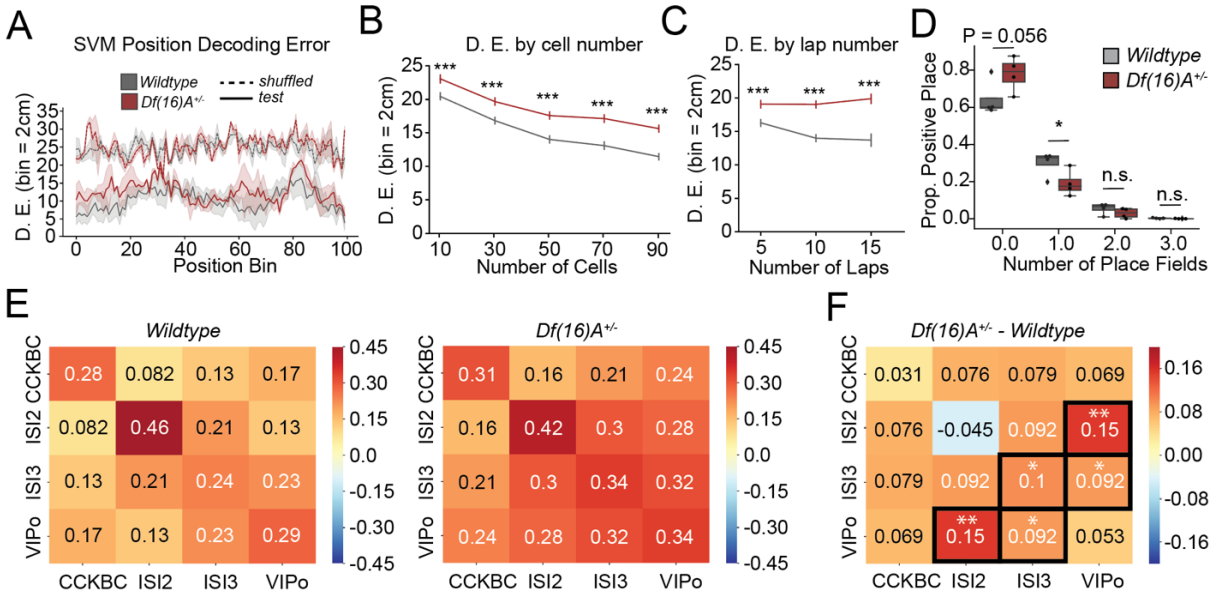

Figure 6. Reduced specificity in *Df(16)A*$^{+/-}$ VIP+ interneuron population activity. A. All recorded VIP+ interneuron activity was used to train a support vector machine (*SVM*) to decode discrete position bins (*D.E.*: decoding error) across the belt. Each bin is equivalent to 2 cm. **B.** SVM results bootstrapped 100 times by number of cells used per genotype per bin. **C.** SVM results bootstrapped 100 times by the number of laps used per genotype per bin. **D.** Proportion of positive place fields detected using the Peak Place method. **E.** Pairwise Pearson's correlation coefficient value matrix between cell types of ($\Delta F/F$) traces across the trial during the Random Foraging paradigm from WT (left) and *Df(16)A*$^{+/-}$ (right). **F.** Comparative differences between cell type correlated activity between genotypes. *CCKBC:* VIP+ and cholecystokinin + basket cell; *ISI3:* Interneuron-selective interneuron type 3; *ISI2:* Interneuron-selective interneuron type 2; *VIPo*: VIP+/Cal-/M2R-/CCK- cells in layer oriens or layer pyramidale. *: P < 0.05. **: P < 0.01. ***: P < 0.001. See Table S1 for detailed statistics.

Discussion

Cognitive dysfunction is central to psychopathology, as many psychiatric conditions share overlapping yet challenging-to-treat cognitive impairments[19–22,40,68]. For instance, schizophrenia often presents with deficits in executive function and working memory[8,12]. Similarly, ASD cases driven by rare damaging mutations[58,99] are frequently associated with pronounced cognitive deficits. Cognitive disabilities are also common in genetic conditions such as 22q11.2 deletion syndrome, where affected individuals frequently display difficulties with attention, working memory, and executive processes[14,67,68]. In this study, we focused on analyzing neuronal impact of rare highly penetrant genetic mutations. The availability of high-quality genetic datasets, each containing dozens of genes with significant disorder associations[1,2,56], now enables direct quantitative comparisons of cell type mutation biases between the disorders. We observed a strong correlation between cell type biases in ASD and SCZ, which was primarily driven by mutations in highly constrained genes. We also identified several cell types that were preferentially affected in each disorder, possibly contributing to disorder-specific symptoms. For example, medium spiny neurons of the striatum showed significantly stronger mutation biases in ASD compared to SCZ, consistent with ASD's core symptoms of repetitive behaviors and social impairments, which have frequently been associated with striatal dysfunction[59,60]. In contrast, multiple interneuron subtypes exhibited stronger mutation biases in SCZ, consistent with recent GWAS-based studies[25,26], particularly parvalbumin-expressing interneurons crucial for gamma oscillations and cognitive processing[100,101], as well as somatostatin-expressing interneurons important for information processing[61]. Supporting these findings, transcriptomic studies have observed alterations in these interneuron populations in SCZ patients[62].

Our genetic analysis revealed dysfunction in CGE-derived GABAergic interneurons as a central vulnerability contributing to cognitive deficits across multiple psychiatric conditions (Figure 3). Specifically, we found that CGE interneurons are more affected in SCZ compared to high-functioning ASD, consistent with cognitive impairments being a core and defining symptom of SCZ[21,22]. We also observed a strong genetic impact on CGE interneurons in low-functioning compared to high-functioning ASD, as well as in intellectual disability and 22q11.2 deletion syndrome. CGE interneurons also showed strong biases in UK Biobank gene sets associated with lower cognitive performance (e.g., verbal-numerical reasoning)[63].

Within the broader class of CGE interneurons, VIP+ subtypes were specifically targeted by genes in the 22q11.2 deletion region, a highly penetrant CNV conferring risk for schizophrenia, ASD, and intellectual disability. To probe the functional consequences, we evaluated VIP+ CGE derived interneuron activity *in vivo* using the *Df(16)A*$^{+/-}$ mouse model. We observed significant defects at both the cellular and circuit levels, likely contributing to broader hippocampal dysfunction previously reported in this mouse model[32,82]. Specifically, VIP+ interneurons exhibited dampened calcium activity, suggesting a reduction in the top-down disinhibition[72,102] normally exerted by these cells in cortical circuits. In addition, we found a reduction in the spatial information carried by their activity. Because synaptic plasticity is critical for fine-tuning synaptic connections and forming dynamic spatial representations and episodic memories, this reduction likely reflects impaired plasticity mechanisms. Such impairment may hinder MGE-derived

interneurons and pyramidal neurons from effectively encoding and updating spatial information[32,82], ultimately disrupting the integration of spatial signals within the hippocampal network. Furthermore, VIP+ interneuron subtypes exhibited increased correlation in their *in vivo* activity, particularly among interneuron-selective interneuron subtypes. This suggests a loss of their normally distinct activity patterns, leading to reduced informational diversity in the circuit. Impaired disinhibition within the CA1 microcircuit in patients with 22q11.2 deletion syndrome likely disrupts the processing and integration of salient inputs, resulting in cognitive deficits associated with hippocampal dysfunction. Given that VIP+ disinhibitory motifs are highly conserved across cortical circuits[70,71,103], the deficits we uncovered in the CA1 circuit are likely pervasive across neocortical brain regions.

Because VIP+ interneurons inhibit other major interneuron subtypes, their activation increases pyramidal neuron excitability, thereby improving the detection of low-contrast signals[89,104]. Thus, these interneurons are essential for learning and attention, as they respond to salient stimuli by adjusting overall neural excitability. For instance, during fear conditioning, blocking VIP+ interneurons disrupts projection neuron activity and impairs fear learning[71]. In the hippocampal CA1 region, proper disinhibitory VIP+ interneuron function is vital for spatial learning as excessive inhibition of pyramidal neurons hinders place cell remapping and performance, while their activation enhances learning outcomes[94]. Similarly, in the prefrontal cortex, activation of VIP+ interneurons improves working memory and attention, whereas activation of Pvalb+, Sst+, or pyramidal neurons often leads to detrimental effects[79,94,104,105]. Of note, impaired disinhibition and CGE-derived VIP+ interneuron dysfunction have also been previously described in other neurodevelopmental disorders[106–108]. In Rett syndrome, for example, selective deletion of Mecp2 in CGE/VIP+ interneurons, but not in Pvalb+ or Sst+ interneurons, leads to deficits in cortical state transitions and social memory[107]. In Dravet syndrome, SCN1A mutations lead to persistent VIP+ interneuron dysfunction in juvenile and adult mutant mice, contributing to social and cognitive deficits[106,108].

While further research is needed to link specific disease-related behaviors to CGE/VIP+ interneuron circuit dysfunction, our combined computational and experimental results suggest that disruption of VIP+ interneuron activity may be a key driver of cognitive deficits in 22q11.2 deletion syndrome and potentially in other cognitively-debilitating neurodevelopmental and psychiatric disorders[109]. These findings position CGE/VIP+ interneurons as a critical point of dysfunction. Given the persistent cognitive comorbidities across multiple psychiatric disorders, pharmacologically targeting CGE interneuron dysfunction is a potential avenue for therapeutic intervention.

METHODS

Rare mutation genetic data for neuropsychiatric disorders and phenotypes

For the analysis on cell type mutation biases of ASD and SCZ, we primarily used the aggregated mutation data obtained from the SFARI Simons Foundation Powering Autism Research for Knowledge (SPARK) cohort and the Schizophrenia Exome Sequencing Meta-Analysis (SCHEMA) cohort. In the SPARK study[2], de novo mutations were identified through familial sequencing of 42,607 ASD probands and 8,267 unaffected siblings. We focused our analysis on de novo likely gene-disrupting (LGD) mutations and damaging missense (Dmis) mutations. Dmis mutations were identified based on the REVEL score[110], which estimates the probability of a missense mutation is pathogenic; mutations with REVEL scores higher than 0.5 were defined as deleterious. For our main analysis, we used 61 genes that reached exome-wide significance (P-value $< 1.3\times10^{-6}$) identified in the SPARK study, using the DeNovoWEST statistical model[56]. In the SCHEMA study[1], which analyzed 24,248 schizophrenia cases and 97,322 controls, to match the number of analyzed ASD genes, we selected the top 61 genes with the strongest association for our analysis (p-value $< 1.0\times10^{-3}$ or FDR < 0.3). Dmis mutations in SCZ were identified based on the MPC score[111], and we included in our analysis LGD and Dmis mutations with MPC scores greater than 3. We also investigated cell type biases across different cohorts with cognitive abnormalities. Specifically, we investigated genes within the 22q11.2 deletion region as defined by Karayiorgou *et al.*[14]. We also analyzed genes associated with verbal-numerical reasoning (VNR) from the UK Biobank study by Chen *et al.*[63]. We separately analyzed genes with positive and negative impacts (indicated by the beta coefficients of gene-phenotype associations), focusing on European population data for optimal statistical power. Additionally, we analyzed genes associated with developmental disorders and intellectual disability (DD/ID) from Kaplanis *et al.*[56], ranking the top genes according to DeNovoWEST p-values.

To validate the robustness of gene set selection, we tested our bias calculations with varying numbers of genes. Our mutation biases were not sensitive to the selection of 61 genes, when different numbers of genes were tested, ranged from top 10 to top 200, ranked by association significance to the disorder, bias correlations with our main selection set remained very strong across a broad range of gene set sizes (Figure S4). We chose 61 genes to balance statistical power from a larger gene set with the individual gene's confidence for association with each disorder.

Human whole brain single-cell data

For our single-cell analysis, we used the recent human brain single-nucleus sequencing dataset [37], comprising 3,369,219 nuclei sampled from 105 regions across the entire brain of three donors. This comprehensive single-cell brain atlas was classified, based on cellular transcriptional similarities and developmental origins, into 461 cell type clusters organized into 31 cell type superclusters.

Gene expression specificity score for individual cell types

To identify neuronal populations preferentially impacted by rare mutations, we calculated a gene expression specificity score for each cell type cluster (Figure S3). To that end, for each gene g in each cell type ct, we first quantified gene expression using Transcripts Per Million (TPM), calculated from raw UMI counts as:

$$TPM_{g,ct} = \frac{UMI_{g,ct}}{\sum_{g'} \mathrm{UMI}_{g',ct}} \times 10^6 \qquad (1)$$

where $UMI_{g,ct}$ is the expression count of gene g in a cell type ct, and the sum in the denominator is across all genes g' in that cell type. In this way, TPM values normalize expression across cell types by accounting for the differences in the total transcript abundance. To filter out genes with very low expression in individual cell types and reduce noise in the specificity calculation, we applied a minimum TPM threshold of 0.1 for each gene in each cell types. Additionally, genes with total UMI counts below 10,000 across all 3 million cells of the human brain cell atlas were excluded from the analysis, removing genes with very low global expression that leads to bad specificity estimate.

Next, we computed a cell type specificity score to quantify how selectively a gene is expressed in each cell type. For each gene g, specificity toward cell type ct was calculated as:

$$S_{g,ct} = n \cdot \frac{\mathrm{TPM}g,ct}{\sum_{ct'} \mathrm{TPM}_{g,ct'}} \qquad (2)$$

where n is the total number of cell types. In case of the uniform expression of a gene across all cell types, the expected value of $S_{g,ct}$ is 1, and higher values indicate stronger cell type specific expression. To prevent extreme values from a small number of genes from dominating downstream bias computations, we capped $S_{g,ct}$ at a maximum of 2, which represents the double of the expected value.

To further ensure comparability across cell types with different expression distributions, we applied a per-cell type centering step. For each cell type, ct, we subtracted the average specificity across all human genes:

$$S'_{g,ct} = S_{g,ct} - \mu_{ct}, \text{ where } \mu_{ct} = \frac{1}{m}\sum_{g=1}^{m} S_{g,ct} \qquad (3)$$

with m denoting the total number of genes. The resulting centered specificity score $S'_{g,ct}$ reflects how strongly a particular gene is enriched in a given cell type relative to all genes in that cell type.

Disorder mutation bias for individual cell types

To calculate cell type-specific mutation biases for each disorder cohort, we weighted gene expression specificities ($S'_{g,ct}$, Equation 3) with their corresponding genetic burdens. This weighted approach accounts for the relative genetic contributions (proportional to the genetic

burden) of individual genes to the disorder. Specifically, for the ASD cohort, we quantified each gene's contribution with the following mutation weight:

$$w_g = n_{g,LGD} + n_{g,Dmis} \qquad (4)$$

where $n_{g,LGD}$ and $n_{g,Dmis}$ are the numbers of observed *de novo* LGD and Dmis mutations in gene g.

For the SCZ cohort, we calculated mutation biases by integrating both *de novo* and inherited mutations identified in case-control studies. Since the genetic evidence comes from these two distinct sources, we computed a mutation counts that combine their contributions. For case-control mutations, the effective count for each gene represents the number of excess mutations in cases after subtracting the expected counts, which were calculated by scaling control mutations by the ratio of the number of cases to controls. We applied this approach separately for each mutation class (LGD and Dmis) and then combined these values with observed *de novo* mutations:

$$n^{eff}_{g,mutType} = n^{case}_{g,mutType} - \frac{n^{ctrl}_{g,mutType}}{N_{ctrl}} \times N_{case} + n^{de\ novo}_{g,mutType} \qquad (5)$$

$$w_g = n^{eff}_{g,LGD} + n^{eff}_{g,Mis3}$$

where $n^{eff}_{g,mutType}$ is the effective count of mutation in gene g, $n^{case}_{g,mutType}$ is number of mutations observed in case cohort in gene g, $n^{ctrl}_{g,mutType}$ is number of mutations observed in controls in gene g. $n^{de\ novo}_{g,mutType}$ is number of de novo mutations in gene g. $mutType$ includes LGD and Mis3 mutations. N_{case} and N_{ctrl} are total number of cases and controls in SCZ cohort, respectively.

For genes associated with the UK Biobank cognitive phenotypes, we utilized each gene's effect size, i.e., beta coefficient from gene-phenotype association tests, as the gene weight. This approach assumes that genes with larger phenotypic effects contribute more strongly to cell type biases relevant to cognition. For genes in the 22q11.2 deletion, we applied uniform weights for all genes (w_g = 1), as each individual gene effectively contributes one LGD mutation to the CNV.

Finally, based on the calculated mutation weights for each gene (Equations 3-5), the mutation bias for all disorder-associated genes toward a cell type ct was calculated as follows:

$$Mutation_Bias_{ct} = \frac{\sum_{g \in G} w_g \cdot S'_{g,ct}}{\sum_{g \in G} w_g} \qquad (6)$$

where the summation is over genes g in the set G containing all implicated genes for a disorder or a phenotype, and w_g is the mutation weight of each gene g.

Statistical significance of the cell type mutation biases

To determine the statistical significance of the calculated cell type mutation biases, we employed a permutation-based framework using matched random gene sets. For each disorder or phenotype, we generated 10,000 random gene sets (selected from genes with valid expression specificity score) matched in size to the target gene set (e.g., ASD, SCZ, DD/ID) and transferred the mutation weights from the original genes to the randomly selected ones. Mutation biases were then computed for each random gene set using the same method as for the original data. At the cluster level (461 cell types), we compared the observed mutation bias of each cluster to the distribution of biases from the 10,000 matched random gene sets. Empirical P-values were calculated per cluster and corrected for multiple comparisons across all 461 clusters using the Benjamini-Hochberg false discovery rate (FDR) procedure.

Sensitivity of the correlation between ASD and SCZ cell type mutation biases to gene properties

To assess how gene-level properties—specifically mutation constraint and expression level—influence the correlation of cell type mutation biases between ASD and SCZ, we evaluated changes in this correlation as a function of these properties. To that end, for each disorder, we independently ranked its associated genes by either mutation constraint or expression level. Gene constraint was quantified using LOEUF scores from the gnomAD v4.0 release [57]; if a gene lacked a LOEUF score in v4.0, we used the corresponding value from gnomAD v2.1. Gene expression levels were obtained from the BrainSpan developmental transcriptome dataset[112], calculated as the average log10 RPKM across all samples. We then iteratively removed genes, one at a time, from each ranked gene list for ASD and SCZ, removing the gene with the highest or the lowest value in each set at each step. This ensured that the number of removed genes remained equal between the two considered disorders. After each step, we recalculated the cell type mutation biases for both ASD and SCZ using the remaining genes and computed the Spearman correlation between their mutation biases across all neuronal cell type clusters. As a control, we also performed 1,000 iterations of random gene removal (matched by number) and computed the corresponding distribution of correlations. This approach allowed us to determine whether the observed similarity between ASD and SCZ cell type biases was primarily driven by genes with high constraint or high expression levels.

Difference in cell type mutation biases between ASD and SCZ

To identify disorder-specific mutational biases at the supercluster level, we assessed the difference in the mutation bias between disorders (ASD vs. SCZ), quantified by the average difference in mutation biases across cell type clusters forming each supercluster. This differential bias measure describing how strongly each particular supercluster is preferentially affected in one disorder compared to another, was calculated as follows:

$$\Delta Bias_{s}^{Pheno_{AB}} = \frac{\sum_{ct_1}^{ct_n}(Bias_{ct}^{Pheno_A} - Bias_{ct}^{Pheno_B})}{n} \qquad (7)$$

where $\Delta Bias_{s}^{Pheno_{AB}}$ is differential bias of supercluster s between phenotype A and B. $Bias_{ct}^{Pheno_A}$ is mutation bias for a cell type cluster in supercluster s for phenotype A, and

$Bias_{ct}^{Phenotype_B}$ is mutation bias for a cell type cluster in supercluster s for phenotype B. The summation is over all *n* cell type clusters within the supercluster.

To evaluate whether these differential biases were statistically significant, we applied the Mann-Whitney U test to compare mutation bias distributions between disorders for each supercluster (e.g., CGE interneurons, MGE interneurons, medium spiny neurons). Multiple hypothesis correction was performed using the Benjamini-Hochberg procedure to control the false discovery rate across 31 superclusters.

Viruses

Cre-dependent recombinant adeno-associated virus (rAAV) for GCaMP7f (rAAV1-syn-FLEX-jGCaMP7f-WPRE, Addgene #1944820-AAV1, titer: ≥1:10^13 vg/mL) and GCaMP8m ((rAAV1-syn-FLEX-jGCaMP8m-WPRE, Addgene # 162378-AAV1, titer: ≥1:10^13 vg/mL) were used to express GCaMP7f or GCaMP8m in the right, dorsal hippocampus of VIP-Cre mice crossed with Df(16)A$^{+/-}$ mice. The Cre-dependent recombinase enabled expression of calcium sensor GCaMP7f or GCaMP8m in VIP+ interneurons (INs).

Viral injections and hippocampal window/headpost implant

During isoflurane anesthesia, Df(16)A$^{+/-}$ x VIP-cre mice were placed onto a stereotaxic surgery instrument. Meloxicam and bupivacaine were administered subcutaneously to reduce discomfort and provide analgesia. The skin was cut along the midline to expose the skull, and a craniotomy was performed over the right hemisphere with a dental drill. A Nanoject injector was loaded with a sterile glass capillary filled with mineral oil and rAAV1-syn-FLEX-jGCaMP7f-WPRE or rAAV1-syn-FLEX-jGCaMP8m-WPRE and lowered into dorsal CA1 of the right hemisphere. Injections were made at AP -2.2, ML -1.75, DV - 1.8, -1.6, -1.4, -1.2, -1.1, -1.0, -0.8 relative to bregma with 64 nl of virus injected at each DV level. The pipette was held within the brain for 5 minutes after the last injection and slowly raised from the brain. The skin was sutured, and a topical antibiotic was applied to the suture site. 1.0 mL of saline was subcutaneously given to each mouse, while the mice recovered in their home cage with a heat pad. Four days after viral injection, a circular cannula with a glass window was inserted into the cavity produced by craniotomy as previously described[113]. Similarly as described above, mice were anesthetized with isoflurane and placed on a stereotaxic surgery instrument. Meloxicam and bupivacaine were subcutaneously given to the mice. The skull was exposed, and a 3 mm craniotomy was performed over the right hippocampus at AP -2.2, ML -1.75 relative to bregma, centered around the injection site. After removal of the dura, the cortex was slowly aspirated with negative pressure and the consistent application of ice-cold cortex buffer. When the horizontal fibers over CA1 were exposed, aspiration was stopped and a sterile collagen membrane was applied to stop bleeding. A 3 mm circular cannula with a glass window was placed into the craniotomy and glued into the site with Vetbond. A headpost was then attached to the posterior of the skull with layers of dental cement. 1.0 mL of saline was subcutaneously given to each mouse, while the mice recovered in their home cage with a heat pad. All mice were monitored for 3 days of post-operative care until behavior training began.

Behavioral training and paradigms

Following the post-op recovery period, mice were acclimated to handling and head-fixation for a few days, while being water restricted to 85-90% of their original weight. Mice were trained to run on a fabric, cue-free burlap belt with random rewards that were automatically dispensed at a decreasing number of random locations. Mice were trained for ~1 week on the cue-free belt and then were transitioned to a cue rich belt during the imaging experiments.

Random Foraging Task:

Water restricted mice were imaged on a cue rich familiar belt for 2 days with 3 random rewards distributed across the length of the belt, randomized every lap.

AOD-based two-photon calcium imaging

After the mice were acclimated and trained in the respective tasks, a high-resolution structural Z-stack was captured 24 hours prior to imaging, while the mouse was anesthetized with isoflurane. The reference Z-stack was used to identify the 3D position of the GCaMP-positive neurons for access by the custom-modified AOD (acousto-optic deflector) microscope (Femto3D-ATLAS, Femtomics Ltd). The AOD microscope was used as previously described in Geiller et al. 2020, and Vancura and Geiller et al. 2023.

To provide stable transmission parameters during chronic imaging in the entire 3D scanning volume, the AOD microscope was extended with a high-speed and precision beam stabilization unit, which was directly attached to the AOD scan head, sensitive to input beam misalignment. The beam stabilization unit consisted of two quadrant detectors (PDQ80A and TPA101, Thorlabs) and two broadband dielectric mirrors (Thorlabs) mounted on motorized mirror mounts (Femtonics). Beam alignment was performed by the LaserControl software (Femtonics).

A water immersion objective (x16 Nikon CF175) was used to focus at the dorsal CA1 pyramidal layer and then fixed in position. A tunable two-photon laser (Coherent Ultra II) was adjusted to wavelength = 920 nm. The high-resolution structural Z-stack was captured in CA1 from ~100 um below to glass to ~500 um to span the entirety of CA1 from the *stratum oriens* to the *stratum lacunosum-moleculare* with a 800x800 pixel capture with a resolution of 1.25 um per pixel with a 4 um step size. Laser power and photomultiplier tube (PMT) detectors (GaAsP, H10770PA-40, Hamamatsu) were compensated in power and gain throughout the Z-stack capture. After the Z-stack was completed, the mouse was returned to its home cage and given 24 hours to recover before functional imaging.

Using the integrated software from Femtonics (MES), the Z-stack was examined, and 100-150 interneurons were manually selected to generate a spreadsheet of the x-y-z positions at the center of each respective cell. These x-y-z positions served as the regions of interest (ROIs) that were then used on subsequent days by the AOD microscope to find the position of the corresponding interneurons. For each day of functional imaging in each mouse, the identical field of view was identified within the CA1 pyramidal layer and then the ROIs were loaded in using the software for AOD 3D imaging. Each imaging session was taken for 10 minutes, with approximately 5-10 Hz for each recording experiment (frame rate depended on the number of ROIs, ROI size, imaging resolution, and scanning speed).

Immunohistochemistry

The immunohistochemical (IHC) staining strategy is consistent with our previously published methods[84,87]. In brief: mice were collected the last day after imaging and perfused with 20 mL Phosphate Buffered Saline (PBS) followed by 20 mL of 4% paraformaldehyde (PFA, Electron Microscopy Sciences) and the brain extracted for overnight fixation in 4% PFA. The next day, the brains were washed 3 x 5 minutes with 1x PBS and subsequently vibratome sliced for horizontal sections from the dorsal side of the brain into 75 µM sections. The relevant sections were then taken through our IHC protocol. Sections were permeabilized for 2 x 20 minutes (0.03% Triton-X 100 (Sigma-Aldrich), 1x PBS), blocked for 45 minutes (0.03% Triton-X 100, 10% Normal Donkey Serum (NDS), 1x PBS), and incubated with primary antibodies (Table 1) for 1 hour at room temperature and overnight at 4 degrees with agitation. After 48 hours, primary antibodies were washed out (3 x 5 minutes 1x PBS) and secondary antibodies were applied for 2 hours (Table 1). Secondary antibodies were removed and the sections were washed with 1x PBS 5 x 15 minutes, and the sections were mounted for confocal imaging.

Cell Marker	Round	Primary Antibody (dilution)	Secondary Antibody (dilution)	Catalog #
Cholecystokinin (CCK)	1	rabbit anti-proCCK (1:500)	donkey anti-rabbit DyLight 405 (1:300)	Frontier Institute CCK-pro-Rb-Af350
Calretinin (CalR)	1	Guinea pig anti-Calretinin (1:1000)	donkey anti-guinea pig Alexa 568 (1:300)	Swant CRgp7
Muscarinic Cholinergic M2 Receptor (M2R)	1	rat anti-M2R (1:2000)	donkey anti-rat Alexa 647 (1:300)	Millipore MAB367

Table 1. Antibodies used in this study

Confocal imaging

The NikonA1 confocal microscope used to take multi-channel fluorescence images (405 nm, 488 nm, 561 nm, and 640 nm excitation for the four blue, green, red and far-red colored channels) of labeled tissue sections. Image capturing yielded 2048 x 2048 pixel z-stacks of the entire depth of the section (with 3 microns between each image of a given stack). Z-stacks were viewable via Fiji (Image J).

Registration of confocal images to *in vivo* z-stacks and identification of immunopositivity/negativity

Unique groupings of cells from *in vivo* z-stacks were used as visual fiducial markers to manually register *ex vivo* 75 µm z-stack images in ImageJ, section by section. Care was taken to note the orientation of the *ex vivo* sections regarding the *in vivo* z-stack images. The coordinates taken from the AOD software when selecting ROIs for imaging against the *in vivo* z-stack were used to identify ROI ID numbers in the registered immunohistochemically stained images.

Assignment of subtype identity based on immunostaining

Interneuron subtypes were assigned based on our previously published classification strategy[84].

Cholecystokinin-expressing basket cells (CCKBCs):
GCaMP-expressing, immunopositive for proCCK, immunonegative for CalR and M2R[114,115]. This population represents perisomatic-targeting basket cells.

Interneuron-selective interneuron type 2 (ISI2s):
GCaMP-expressing, immunonegative for CalR, CCK and M2R. Present in *stratum radiatum* or *stratum lacunosum moleculare* CA1 layers[114,115].

Interneuron-selective interneuron type 3 (ISI3s):
GCaMP-expressing, immunopositive for CalR and immunonegative for CCK and M2R. Present in all CA1 layers[104,114–117].

VIP only (VIPos):
GCaMP-expressing, immunonegative for CalR, CCK and M2R. Present in *stratum oriens* or *stratum pyamidale* CA1 layers. This category excludes CCKBCs, ISI2s, and ISI3s, and could possibly include long-range projecting interneurons[118], but it may not be restricted to them; therefore we called them VIP only for our purposes in this study.

Pre-processing of Ca2+ imaging data
Raw movies of each individual cell were independently motion corrected using the whole-frame cross registration implemented in the SIMA package[119]. ROIs were then hand-drawn over each imaged cell. Fluorescence was extracted from each drawn ROI using SIMA. DeltaF/F was then computed based on a 1st percentile baseline value over a 30-second rolling window. The DeltaF/F traces were then smoothed through an exponential filter. For analyses involving velocity regressed traces, each animal's velocity was smoothed with a Hanning filter and then covariate linear regression was applied to each fluorescence trace where the smoothed velocity is regressed out.

Velocity Correlation
For each cell, velocity correlation was computed by taking Pearson's correlation coefficient between the DeltaF/F trace and animal's smoothed velocity with a -5 second to +5 second rolling lag. The highest absolute value of the correlation coefficients in this time window was taken as the correlation coefficient for the respective cell.

Peri-Event Time Averages (PETA)
For salient stimuli such as reward distribution events, a PETA was constructed around each event respectively. These events were z-score and then averaged for each respective cell, and the z-scored averages were visualized using a heatmap or an averaged line-plot. A Post-Pre metric was calculated based on the z-scored averages as a measure for event modulation.

Spatial Tuning Curve
The 2 meter belt was divided into 100 bins (~2cm per bin). Spatial tuning curves for each cell during an experiment were generated by averaging the velocity regressed DeltaF/F in each bin, when the animal was running over 5 cm/s.

Place field calculation

The spatial tuning curves were shuffled 1000 times by circularly rotating the velocity-regressed ΔF/F tuning curves around the 100 spatial bins to generate a shuffle distribution. Cells were classified as being spatially selective (i.e., having a place field) if the cell's tuning curve exceeded the 95th percentile (or was under the 5th percentile for negatively selective cells) with at least 10 sequential bins over/under the cutoffs from the shuffled distribution. The number of bins over or under the 95th and 5th percentile curves were visualized and a cutoff of 30 consecutive bins was used for the figures as it represented the approximate 75th quartile for place field width.

Position Decoding

A linear classifier support vector machine (SVM) was trained on the tuning curves of each respective cell and the decoding error was visualized. The SVM was cross-validated by training the classifier on (n-1) laps and evaluating on the held-out lap and this process was repeated such that every lap was utilized as a test lap at least once. Furthermore, the SVM was bootstrapped with different numbers of input cells and input laps to compare the position decoding efficacy between genotypes.

Cross-correlation Analysis

Pairwise Pearson's correlation coefficients were computed for every pair of cells within a given experiment. The average coefficient value for each subtype was then calculated per trial pair and averaged across mice.

Transient Analysis

Online Active Set method to Infer Spikes (OASIS) was used to generate deconvolved spike events based on transient events within the dF/F traces[96]. We understand that these are not true spiking events, and we are using OASIS to algorithmically identify transient events rather than interpret the deconvolved spiking events.

Frequency: The deconvolved events were filtered to remove events that were within 10 frames. The total number of filtered deconvolved events by OASIS was normalized by the total duration of the recording.

For each cell, the average transient was segmented within a 15-second time window and computed by averaging along aligned deconvolved spike times. If multiple detected events were within 10 frames, the events were treated as a single transient. A cell was only used if there were at least 3 detected transients within the total trace to exclude cells without obvious GCaMP-Ca^{2+} dynamics. For each average transient, we computed the median value based on 5 seconds pre peak transient and the range 5-10 seconds after the peak transient (given that the average transient took significantly less than 5 seconds to resolve) to act as the baseline.

Amplitude: The difference between the max value of the average transient and the baseline value was computed

QUANTIFICATION AND STATISTICAL ANALYSIS

Statistical analyses

Subtype comparisons were conducted using one-way ANOVA tests with Tukey's range tests with correction for multiple testing if appropriate. For comparisons across genotypes, unpaired t tests were utilized if the data followed a normal distribution. Otherwise, for non-normally distributed comparisons, the Mann-Whitney U test was used. *, $P < 0.05$, **, $P < 0.01$, ***, $P < 0.001$. All data analysis and visualization were done with custom software built on Python version 2.7.15.

Code and Data availability:

All data used in this report are publicly available. ASD genes and mutations counts can be found in Supplementary table from Zhou et al[2]. SCZ genes and mutation counts can be found in Supplementary table from Singh et al[1]. DD/ID genes and mutations counts can be found in Supplementary table from Kaplanis et al[56]. Genes implicated in UKBB adult cognitive functions can be found in Supplementary table from Chen et al[63]. Genes in 22q11.2 3Mb deletion and 1.5 Mb deletion can be found in Karayiorgou et al[14]. Human brain cell atlas can be found (https://cellxgene.cziscience.com/collections/283d65eb-dd53-496d-adb7-7570c7caa443). Individual genetics and phenotypic data used in our study from the SPARK project are available through the Simons Foundation (https://base.sfari.org) following the access procedures described in Zhou et al. Gene constraint score from gnomAD can be found at (https://gnomad.broadinstitute.org/news/2024-03-gnomad-v4-0-gene-constraint/). Brainspan expression data can be found at (https://www.brainspan.org/).

The code used for our implementation of the Cell type bias with analysis pipeline, and code to generating all figures and tables, is available on GitHub: (https://github.com/explorerwjy/CellTypeBias_VIP.git).

Acknowledgements

S.A.H. is supported by the Burroughs Welcome grant. This work has been supported by the grants NIMHR01MH124923 to D.V. and J.A.G, NIMHR01MH124047 to J.A.G, Stavros Niarchos Foundation to J.A.G., and NIMHR01MH124047 NIMHR01MH124867 NINDSR01NS133381 to A.L. We thank members of the Gogos, Losonczy, and Vitkup labs for fruitful scientific discussions.

Author Contributions

S.H., J.W., J.A.G., A.L., and D.V. conceived the study. J.W. and J.C. performed genetic bias and computational analyses. S.H. and B.R. collected and analyzed experimental data. S.H., J.W., J.A.G., A.L., and D.V. wrote the manuscript.

Supplemental Tables and Figures

Figure	Statistics
5C	*CCKBC:* CCK basket cells student's t-test: T statistic: -1.313, P = 0.02. *ISI3*: Interneuron-Selective Interneuron Type 3: Student's T test Statistic: -3.284, P = 0.001. *ISI2:* Interneuron-Selective Interneuron Type 2: Student's T test Statistic: 2.191, P = 0.03. *VIP+ Alone:* Student's T-test Statistic: 1.105, P = 0.3
5E	Mann-Whitney test, t = 104931.0, P = 4×10^{-5}.
5G	Mann-Whitney test, t =24290.0, P = 0.04.
5I	Mann-Whitney test, t = 42011.0, P = 2×10^{-13}.
5J	Mann-Whitney test, t = 54521.5, P = 1×10^{-3}
5L	*CCKBC*: cholecystokinin-expressing basket cells Mann-Whitney U test: P = 0.3, *ISI3*: interneuron-selective interneuron type 3 cells Mann-Whitney U test: P = 0.0029, *ISI2*: interneuron-selective interneuron type 2 cells Mann-Whitney U test: P = 0.003, *VIP-Alone*: Mann-Whitney U test: P = 0.04. For Mann Whitney U tests: median ± inter-quartile range.
6A	Averaged per animal: Mann-Whitney U test: statistic = 3.5, P = 0.144
6B	10 cells: Mann-Whitney U test: P = 6×10^{-10}, 30 cells: Mann-Whitney U test: P = 8×10^{-11}, 50 cells: Mann-Whitney U test: P = 3×10^{-16}, 70 cells: Mann-Whitney U test: P = 4×10^{-18}8, 90 cells: Mann-Whitney U test: P = 3×10^{-21}.
6C	5 laps: Mann-Whitney U test: P = 3×10^{-6}, 10 laps: Mann-Whitney U test: P =2×10^{-21}, 15 laps: Mann-Whitney U test: P =3×10^{-15}.
6D	0 fields: Mann-Whitney U test: p = 0.056, 1 field: Mann-Whitney U test: P = 0.03, 2 fields: Mann-Whitney U test: P = 0.1, 3 fields: Mann-Whitney U test: P = 0.06.
6F	Welch's T-test comparisons: ISI2 vs VIPo: P = 0.007. ISI3 vs ISI3: P = 0.043. ISI3 vs VIPo: P = 0.04. VIPo vs ISI2: P = 0.007. VIPo vs ISI3: P = 0.04. Welch's T-test.

Table S1: Statistical detail summary.
Boxplots show the 25th, 50th (median), and 75th quartile ranges, with the whiskers extending to 1.5 interquartile ranges below or above the 25th or 75th quartiles, respectively. Outliers are defined as values extending beyond. the whisker ranges. For Welch's t tests: mean ± sem. For Mann Whitney U tests: median ± inter-quartile range. n.s.: not significant. *: P < 0.05. **: P < 0.01. ***: P < 0.001.

Table S2-S7: Human brain Cell type biases at cluster level for different psychiatric disorders and traits, including SCZ, ASD, ASD with ID, DD/ID, 22q11.2 and VNR- genes.

Table S8-S11: Human brain Cell type biases Bias contrast at supercluster level of different comparisons, including ASD to SCZ, ASD to ASD with ID, ASD to DD/ID, and VNR- to VNR+.

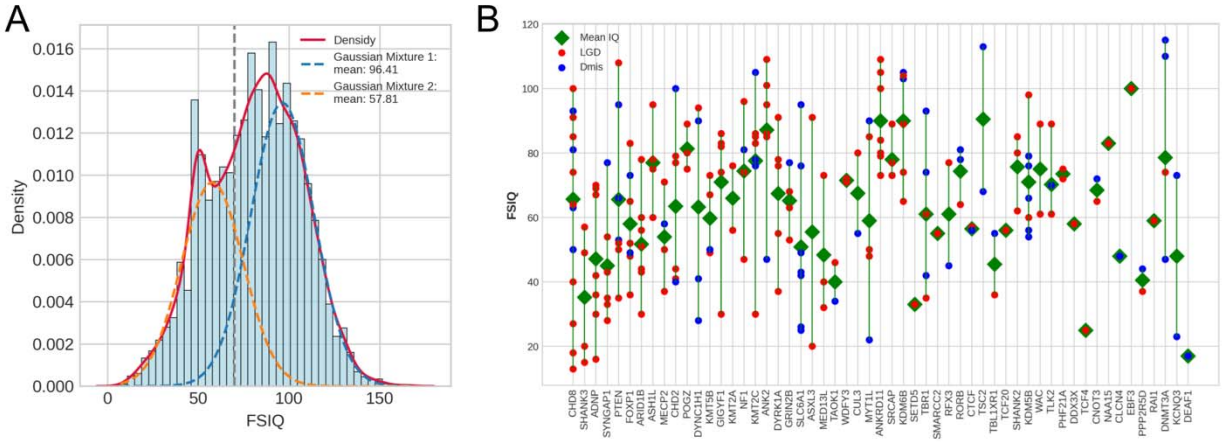

Figure S1: Full-scale IQ distribution among ASD probands in the SPARK and ASC cohorts. A). The distribution of FSIQ scores among ASD probands from the SPARK and ASC cohorts. The histogram (blue bars) shows the FSIQ distribution with an overlaid density plot (red line). A two-component Gaussian mixture model was fitted to the data

(blue and orange dashed curves), revealing distinct subpopulations within the FSIQ distribution. The vertical dashed line at FSIQ = 70 indicates a commonly used threshold for intellectual disability (IQ < 70). FSIQ phenotype data of SPARK and ASC probands were obtained from SFARI base and Satterstrom *et al.*[120] **B).** Gene-specific FSIQ patterns across the top 61 high-confidence ASD genes, represented by vertical lines. Individual probands are represented as dots, colored by mutation type, with likely gene-disrupting (LGD) mutations in red and damaging missense (Dmis) mutations in blue. The green diamonds indicate the average FSIQ in the cohorts for each gene. Genes are arranged along the x-axis in based on *de novo* west P-values from Zhou *et al.*[2].

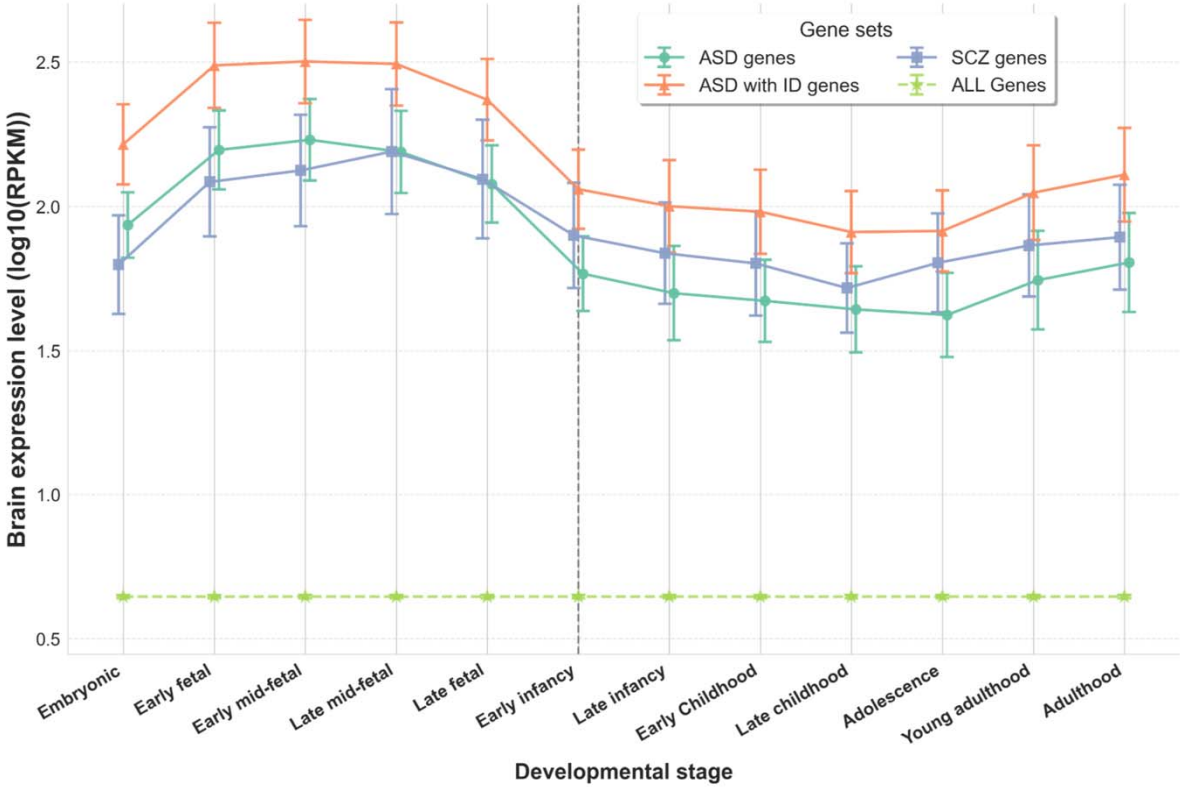

Figure S2. Temporal expression patterns of disorder-associated genes across human brain development stages. Average expression levels (log10 RPKM) of genes associated with different disorders across human brain developmental stages, from embryonic to adult periods. Gene sets include ASD genes (green), ASD with ID genes (orange), SCZ genes (blue), and all human genes (dashed yellow). Error bars represent standard error of the mean. SCZ genes show similar expression levels to ASD genes, while ASD with ID genes show higher expression levels. The vertical dashed line marks the transition from prenatal to postnatal periods. Expression data were obtained from the BrainSpan Atlas of Human Brain Development[112].

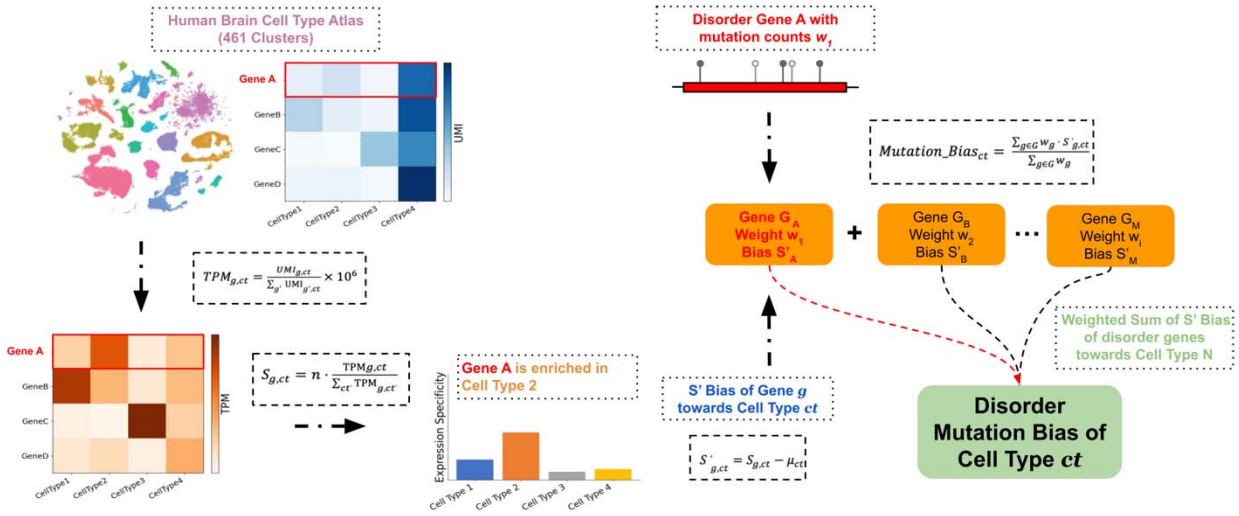

Figure S3. Workflow for computing cell type mutation biases from disorder-associated genes.
This schematic illustrates the updated two-step procedure used to compute disorder mutation bias for each brain cell type. **(Left)**: Starting from a comprehensive single-cell gene expression atlas of 461 human brain cell types, we first compute gene expression levels as TPM (transcripts per million) for each gene across all cell types. Expression specificity scores are then derived by normalizing each gene's TPM in a given cell type relative to its total TPM across all cell types. **(Right)**: For each disorder, cell type–specific mutation bias is calculated by aggregating expression specificity scores across all disorder-associated genes, weighted by their mutational burden. This yields a composite mutation bias score for each cell type, reflecting its relative vulnerability to rare pathogenic mutations in the disorder.

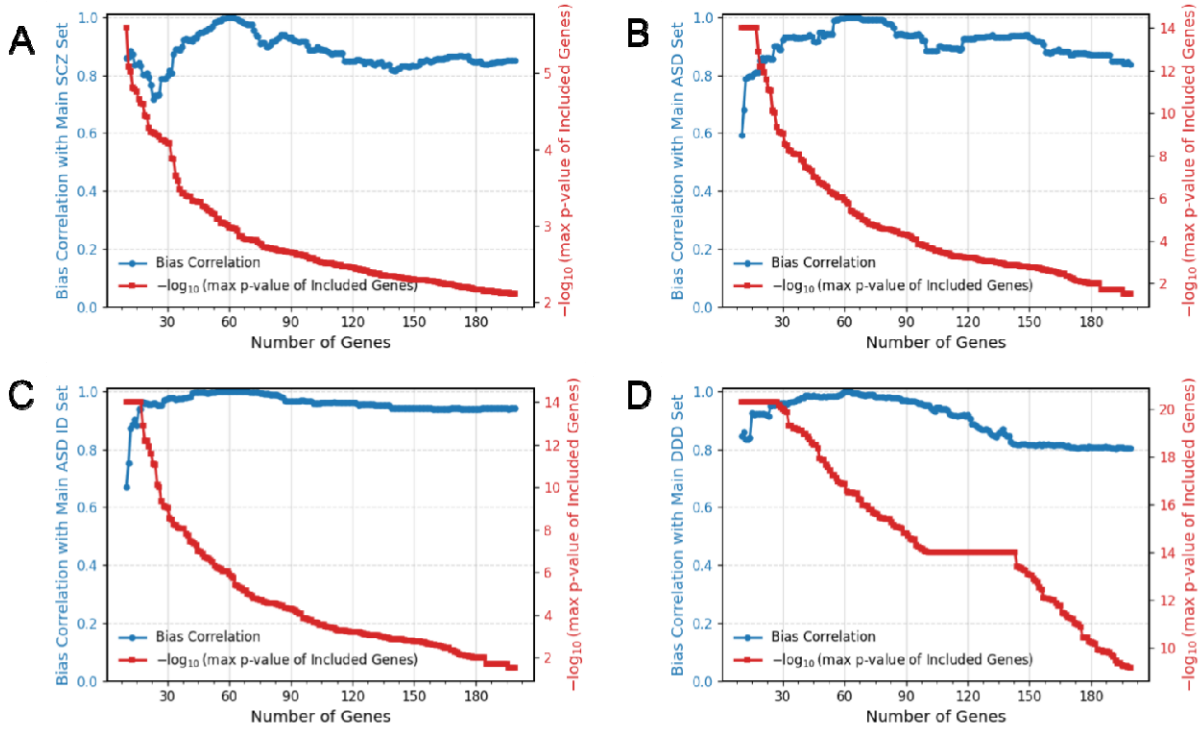

Figure S4. Impact of number of genes included in the mutation bias analysis. Mutation bias correlations were calculated between the primary gene set (61 genes) and gene sets of varying sizes (10–200 genes). For each disorder, cell type–specific biases were recalculated while progressively increasing the number of genes included, starting from the most significantly associated and adding progressively less significant genes. Panels show results for: **A)** SCZ; **B)** ASD; **C)** ASD with ID and **D)** DDD. Blue lines indicate the Spearman correlation between the mutation bias profile of the expanded set and the primary 61-gene set; red lines indicate the –log10 (P-value) of the least significant gene included in the set.

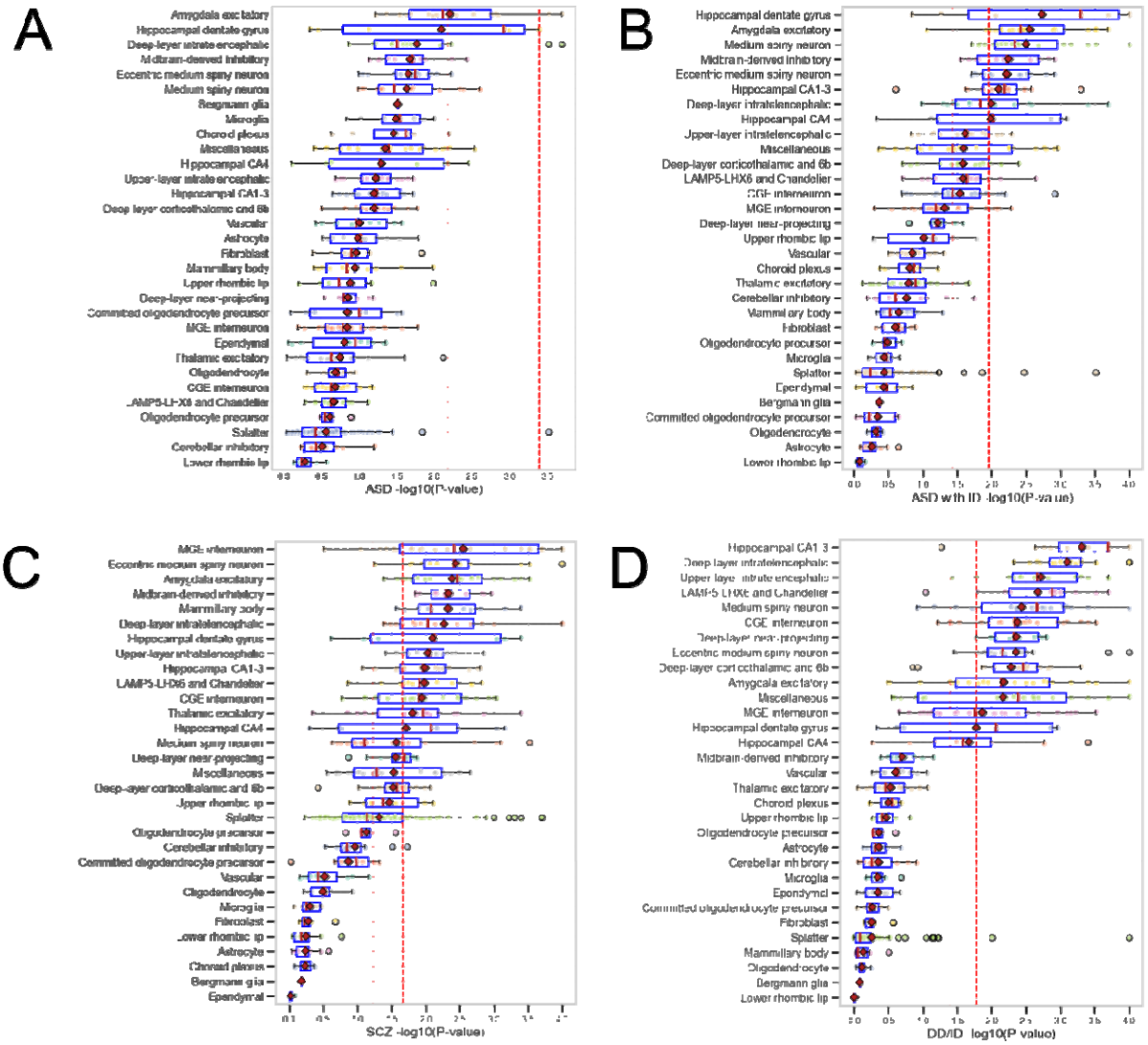

Figure S5. Comprehensive analysis of mutation biases across brain cell types in psychiatric disorders. Box plots show the distribution of mutation bias significance ($-\log_{10}(P)$) for major brain cell type superclusters in: **A)** ASD, **B)** ASD with intellectual disability (ID), **C)** schizophrenia (SCZ), and **D)** developmental disorders and intellectual disability (DD/ID). Each point represents a cell type (cluster) within a given supercluster. P-values were calculated by comparing the observed mutation bias of each cluster to a null distribution generated from 10,000 random gene sets (see Methods). Red diamonds indicate the average $-\log_{10}(P)$ for each supercluster, and red vertical lines indicate the median. The red dashed line corresponds to an FDR threshold of 0.05; the lighter red dashed line corresponds to FDR = 0.1.

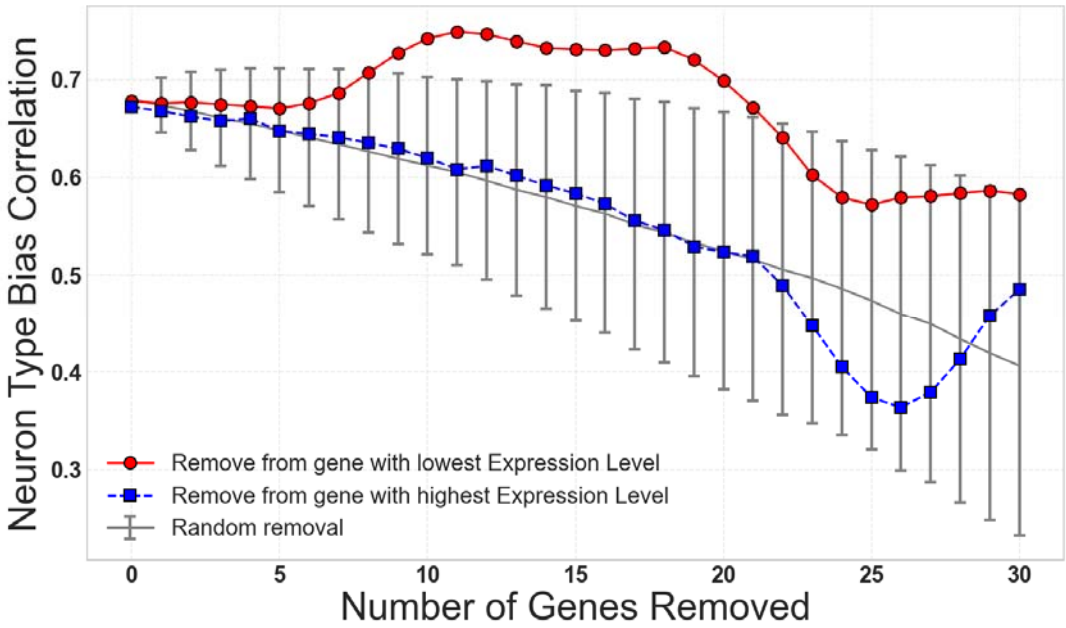

Figure S6. Impact of gene expression levels on ASD-SCZ cell type bias correlation. Effect of sequentially removing genes based on their expression levels (based on brain span expression[112]) on the cell type mutation bias correlation between ASD and SCZ. Red line shows correlation changes when removing genes with lowest expression levels first, while blue dashed line shows removal of highest expressing genes first. Grey line and error bars show mean ± standard deviation for random gene removal.

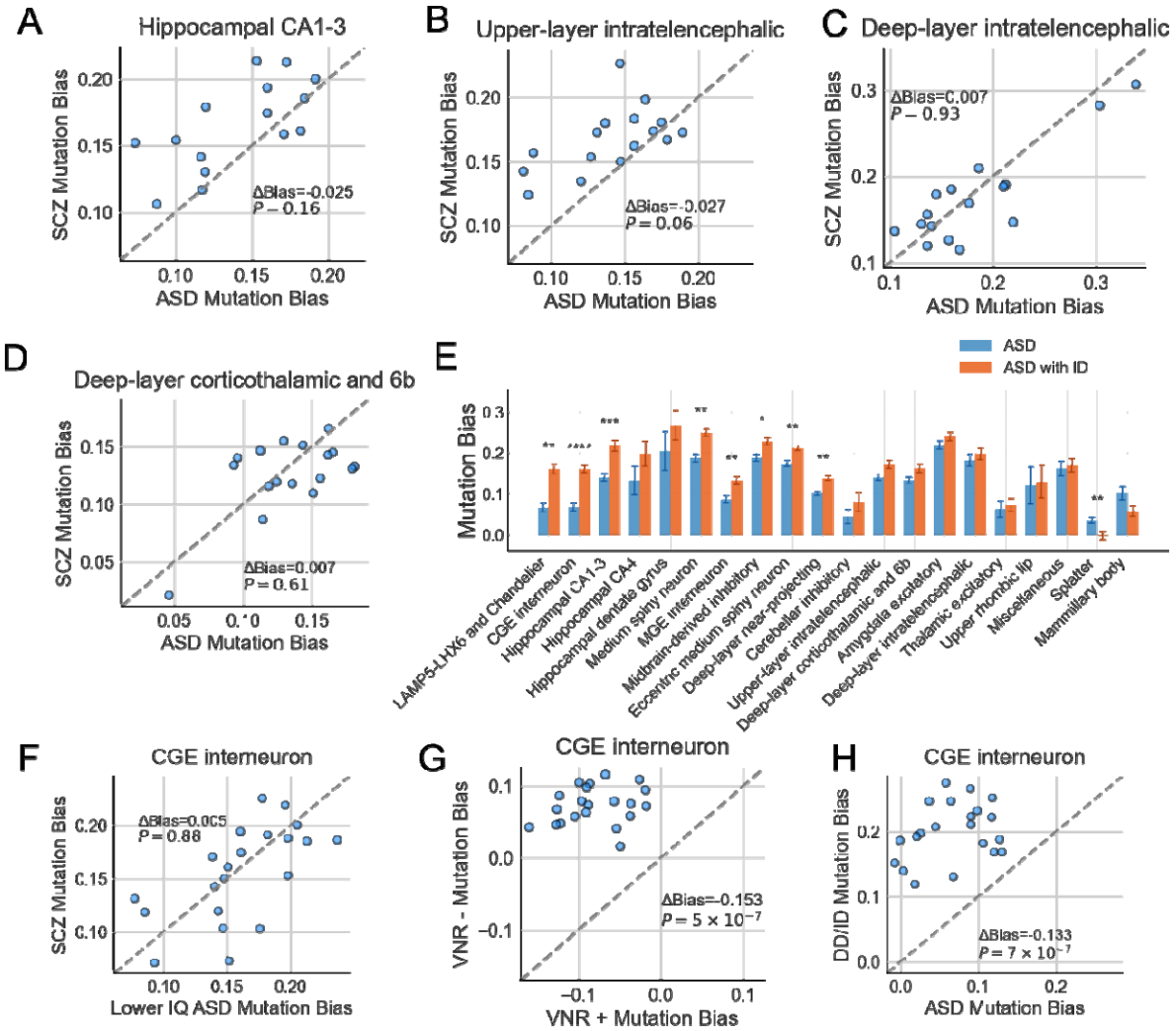

Figure S7. ASD and SCZ Mutation bias towards different cell type superclusters. A-D. Detailed comparison of mutation biases in specific neuron superclusters between ASD and SCZ, P-value was calculated based on Mann–Whitney U test with FDR correction: **(A)** Hippocampal CA1-3 neurons. **(B)** Upper-layer IT. **(C)** Deep-layer IT **(D)** Deep-layer corticothalamic and 6b neurons. **(E)** Bar plot comparing mutation biases across major neuron types between ASD (blue) and ASD with ID (orange). Asterisks indicate significance level between groups (*: P < 0.05. **: P < 0.01. ***: P < 0.001, ****: P < 0.0001, Mann–Whitney U test with FDR correction). All neuronal cell types at supercluster level is displayed. Error bars represent standard error across clusters from corresponding supercluster. **(F)** CGE interneurons show similar bias in SCZ genes compared to ASD with ID genes. **(G)** CGE interneurons show stronger bias in VNR- genes compared to VNR+ genes (verbal-numerical reasoning negative and positively associated genes). **(H)** CGE interneurons show stronger bias in DD/ID genes compared to ASD genes.

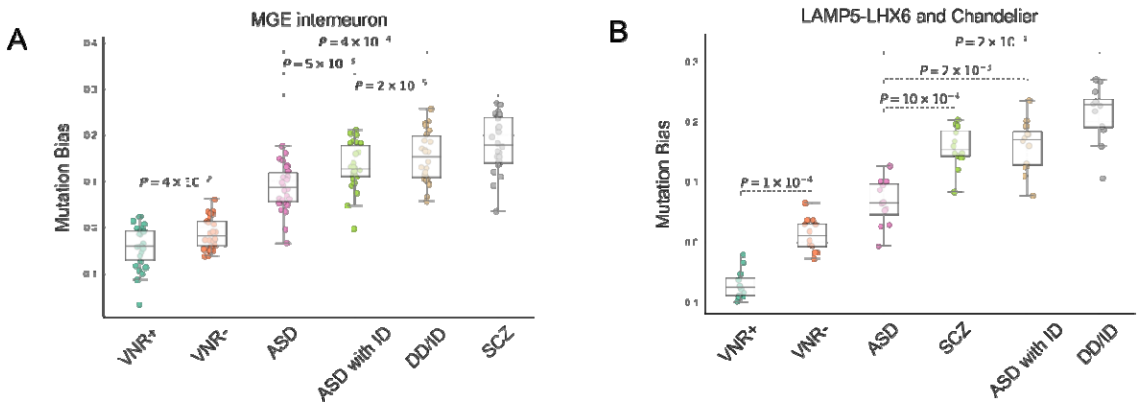

Figure S8. Mutation bias comparison across psychiatric disorders for MGE interneurons and LAMP5-LHX6/Chandelier interneurons. **A**: Mutation bias distribution for MGE interneurons across different cohorts. **B**: Mutation bias distribution for LAMP5-LHX6 and Chandelier cells across different cohorts. P-values for pairwise comparison were shown, Mann–Whitney U test with FDR correction.

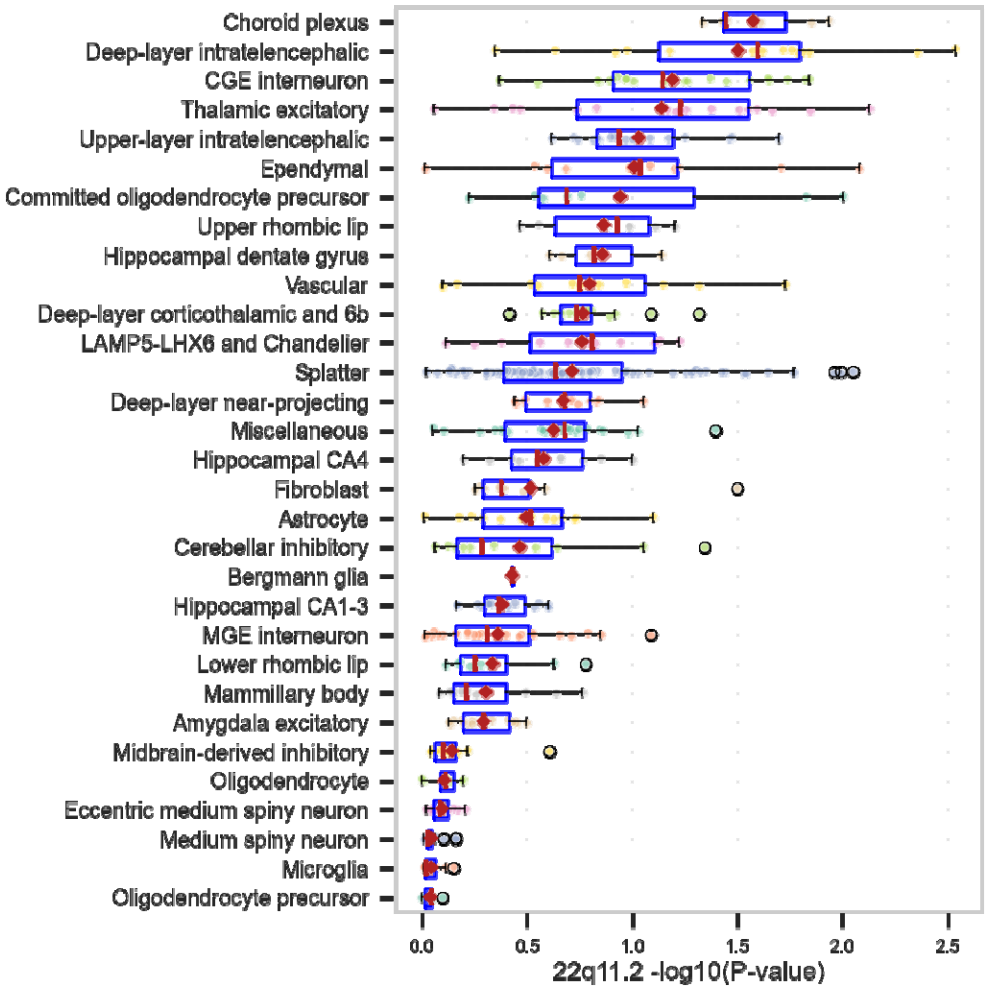

Figure S9. Comprehensive analysis of mutation biases across brain cell types in 22q11.2 deletion. Box plots showing significance of mutation biases for all major brain cell types (superclusters). Each bar represents the bias distribution of the human adult brain neuron type belonging to a supercluster, X-axis shows the significance of biases as -log10(P-value). Red diamond shows average of each supercluster, red vertical line shows medium of each supercluster.

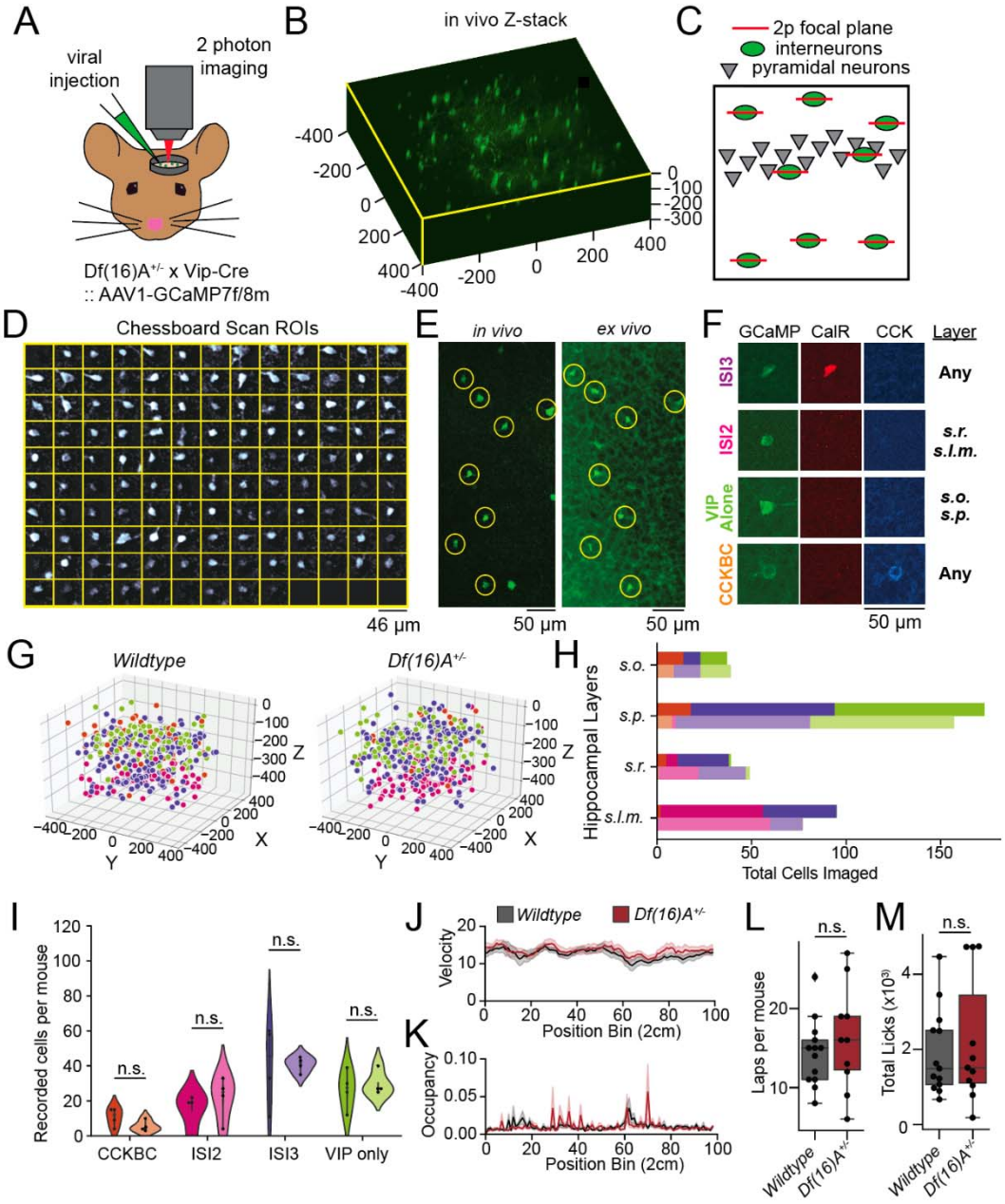

Figure S10. VIP+ Cell imaging and targeting strategy.

A. Schematic for mouse crossing and viral injection and calcium imaging setup. **B.** 3D reconstruction of Z-stack from VIP-cre mice **C.** Schematic of 3D regions of interest (ROIs) imaged with AOD 2-photon microscopy. **D.** Example chessboard scan view of imaged ROIs. **E.** Manual registration of *in vivo* Z-stack section with *ex vivo* 75 □m transverse section for *post hoc* subtype classification with immunohistochemistry. **F.** Histological strategy for defining VIP-expressing cell subtypes. **G.** 3D distribution of all cells imaged from both genotypes. **H.** Distribution of VIP+ subtypes across CA1 hippocampal layers. **I.** Number of cells recorded per mouse (n=4, ISI3: ISI2: VIP+ Alone: CCKBC:). **J.** Average velocity in cm per second plotted by location on the belt of WT (black) and *Df(16)A*$^{+/-}$ (brown) mice. **K.** Average percent occupancy on the belt by position per genotype plotted by location on the belt of WT (black) and *Df(16)A*$^{+/-}$ (brown) mice. **L.** Total laps across mice within genotype (WT: 14.4 ± 1.1 laps, *Df(16)A*$^{+/-}$: 16.2 ± 2.0 laps, Mann Whitney U = 51.5, P = 0.2). **M**. Licking proportion of WT (black) and *Df(16)A*$^{+/-}$ (brown). There is no

significant difference in total licks across the belt during Random Foraging in WT (n = 4) or *Df(16)A*$^{+/-}$ (n = 4) depicted by box-and-whisker plot, WT: 1916 ± 304 licks, *Df(16)A*$^{+/-}$: 2200 ± 489 licks, Mann-Whitney U Test, P = 0.4.

References

1. Singh, T., Poterba, T., Curtis, D., Akil, H., Al Eissa, M., Barchas, J.D., Bass, N., Bigdeli, T.B., Breen, G., Bromet, E.J., et al. (2022). Rare coding variants in ten genes confer substantial risk for schizophrenia. Nature *604*, 509–516.

2. Zhou, X., Feliciano, P., Shu, C., Wang, T., Astrovskaya, I., Hall, J.B., Obiajulu, J.U., Wright, J.R., Murali, S.C., Xu, S.X., et al. (2022). Integrating de novo and inherited variants in 42,607 autism cases identifies mutations in new moderate-risk genes. Nat. Genet. *54*, 1305–1319.

3. Gilman, S.R., Chang, J., Xu, B., Bawa, T.S., Gogos, J.A., Karayiorgou, M., and Vitkup, D. (2012). Diverse types of genetic variation converge on functional gene networks involved in schizophrenia. Nat. Neurosci. *15*, 1723–1728.

4. Gilman, S.R., Iossifov, I., Levy, D., Ronemus, M., Wigler, M., and Vitkup, D. (2011). Rare de novo variants associated with autism implicate a large functional network of genes involved in formation and function of synapses. Neuron *70*, 898–907.

5. Gandal, M.J., Haney, J.R., Parikshak, N.N., Leppa, V., Ramaswami, G., Hartl, C., Schork, A.J., Appadurai, V., Buil, A., Werge, T.M., et al. (2018). Shared molecular neuropathology across major psychiatric disorders parallels polygenic overlap. Science *359*, 693–697.

6. Rees, E., Creeth, H.D.J., Hwu, H.-G., Chen, W.J., Tsuang, M., Glatt, S.J., Rey, R., Kirov, G., Walters, J.T.R., Holmans, P., et al. (2021). Schizophrenia, autism spectrum disorders and developmental disorders share specific disruptive coding mutations. Nat. Commun. *12*, 5353.

7. Kaladjian, A., Jeanningros, R., Azorin, J.-M., Anton, J.-L., and Mazzola-Pomietto, P. (2011). Impulsivity and neural correlates of response inhibition in schizophrenia. Psychol. Med. *41*, 291–299.

8. Trevisan, D.A., Foss-Feig, J.H., Naples, A.J., Srihari, V., Anticevic, A., and McPartland, J.C. (2020). Autism spectrum disorder and schizophrenia are better differentiated by positive symptoms than negative symptoms. Front. Psychiatry *11*, 548.

9. Andreasen, N.C., and Olsen, S. (1982). Negative v positive schizophrenia. Definition and validation. Arch. Gen. Psychiatry *39*, 789–794.

10. Forbes, N.F., Carrick, L.A., McIntosh, A.M., and Lawrie, S.M. (2009). Working memory in schizophrenia: a meta-analysis. Psychol. Med. *39*, 889–905.

11. Green, M., and Walker, E. (1985). Neuropsychological performance and positive and negative symptoms in schizophrenia. J. Abnorm. Psychol. *94*, 460–469.

12. Spek, A.A., and Wouters, S.G.M. (2010). Autism and schizophrenia in high functioning adults: Behavioral differences and overlap. Res. Autism Spectr. Disord. *4*, 709–717.

13. Schneider, M., Debbané, M., Bassett, A.S., Chow, E.W.C., Fung, W.L.A., van den Bree, M., Owen, M., Murphy, K.C., Niarchou, M., Kates, W.R., et al. (2014). Psychiatric disorders from childhood to adulthood in 22q11.2 deletion syndrome: results from the International

Consortium on Brain and Behavior in 22q11.2 Deletion Syndrome. Am. J. Psychiatry *171*, 627–639.

14. Karayiorgou, M., Simon, T.J., and Gogos, J.A. (2010). 22q11.2 microdeletions: linking DNA structural variation to brain dysfunction and schizophrenia. Nature Reviews Neuroscience 2010 11:6 *11*, 402–416.

15. Rees, E., Kendall, K., Pardiñas, A.F., Legge, S.E., Pocklington, A., Escott-Price, V., MacCabe, J.H., Collier, D.A., Holmans, P., O'Donovan, M.C., et al. (2016). Analysis of intellectual disability copy number variants for association with schizophrenia. JAMA Psychiatry *73*, 963–969.

16. Miller, D.T., Adam, M.P., Aradhya, S., Biesecker, L.G., Brothman, A.R., Carter, N.P., Church, D.M., Crolla, J.A., Eichler, E.E., Epstein, C.J., et al. (2010). Consensus statement: chromosomal microarray is a first-tier clinical diagnostic test for individuals with developmental disabilities or congenital anomalies. Am. J. Hum. Genet. *86*, 749–764.

17. Ropers, H.H. (2008). Genetics of intellectual disability. Curr. Opin. Genet. Dev. *18*, 241–250.

18. Vissers, L.E.L.M., Gilissen, C., and Veltman, J.A. (2016). Genetic studies in intellectual disability and related disorders. Nat. Rev. Genet. *17*, 9–18.

19. Millan, M.J., Agid, Y., Brüne, M., Bullmore, E.T., Carter, C.S., Clayton, N.S., Connor, R., Davis, S., Deakin, B., DeRubeis, R.J., et al. (2012). Cognitive dysfunction in psychiatric disorders: characteristics, causes and the quest for improved therapy. Nat. Rev. Drug Discov. *11*, 141–168.

20. Harvey, P.D., and Strassnig, M. (2012). Predicting the severity of everyday functional disability in people with schizophrenia: cognitive deficits, functional capacity, symptoms, and health status. World Psychiatry *11*, 73–79.

21. Bowie, C.R., and Harvey, P.D. (2006). Cognitive deficits and functional outcome in schizophrenia. Neuropsychiatr. Dis. Treat. https://doi.org/10.2147/nedt.s24531.

22. Bowie, C.R., Reichenberg, A., Patterson, T.L., Heaton, R.K., and Harvey, P.D. (2006). Determinants of real-world functional performance in schizophrenia subjects: Correlations with cognition, functional capacity, and symptoms. Am. J. Psychiatry *163*, 418–425.

23. Trubetskoy, V., Pardiñas, A.F., Qi, T., Panagiotaropoulou, G., Awasthi, S., Bigdeli, T.B., Bryois, J., Chen, C.Y., Dennison, C.A., Hall, L.S., et al. (2022). Mapping genomic loci implicates genes and synaptic biology in schizophrenia. Nature *604*, 502–508.

24. Bryois, J., Skene, N.G., Hansen, T.F., Kogelman, L.J.A., Watson, H.J., Liu, Z., Eating Disorders Working Group of the Psychiatric Genomics Consortium, International Headache Genetics Consortium, 23andMe Research Team, Brueggeman, L., et al. (2020). Genetic identification of cell types underlying brain complex traits yields insights into the etiology of Parkinson's disease. Nat. Genet. *52*, 482–493.

25. Duncan, L.E., Li, T., Salem, M., Li, W., Mortazavi, L., Senturk, H., Shahverdizadeh, N., Vesuna, S., Shen, H., Yoon, J., et al. (2025). Mapping the cellular etiology of schizophrenia and complex brain phenotypes. Nat. Neurosci., 1–11.

26. Yao, S., Harder, A., Darki, F., Chang, Y.-W., Li, A., Nikouei, K., Volpe, G., Lundström, J.N., Zeng, J., Wray, N., et al. (2025). Connecting genomic results for psychiatric disorders to human brain cell types and regions reveals convergence with functional connectivity. Nature Communications. https://doi.org/10.1101/2024.01.18.24301478.

27. Broglio, C., Martín-Monzón, I., Ocaña, F.M., Gómez, A., Durán, E., Salas, C., and Rodríguez, F. (2015). Hippocampal pallium and map-like memories through vertebrate evolution. J. Behav. Brain Sci. *05*, 109–120.

28. Rodríguez, F., López, J.C., Vargas, J.P., Broglio, C., Gómez, Y., and Salas, C. (2002). Spatial memory and hippocampal pallium through vertebrate evolution: insights from reptiles and teleost fish. Brain Res. Bull. *57*, 499–503.

29. Buzsáki, G. (2002). Theta oscillations in the hippocampus. Neuron *33*, 325–340.

30. Pelkey, K.A., Vargish, G.A., Pellegrini, L.V., Calvigioni, D., Chapeton, J., Yuan, X., Hunt, S., Cummins, A.C., Eldridge, M.A.G., Pickel, J., et al. (2023). Evolutionary conservation of hippocampal mossy fiber synapse properties. Neuron *111*, 3802-3818.e5.

31. Hamm, J.P., Peterka, D.S., Gogos, J.A., and Yuste, R. (2017). Altered Cortical Ensembles in Mouse Models of Schizophrenia. Neuron *94*, 153-167.e8.

32. Herrlinger, S.A., Rao, B.Y., Conde Paredes, M.E., Tuttman, A.L., Arain, H., Varol, E., Gogos, J.A., and Losonczy, A. (2024). Disorganized Inhibitory Dynamics and Functional Connectivity in Hippocampal area CA1 of 22q11.2 Deletion Mutant Mice. bioRxiv, 2024.04.28.591464. https://doi.org/10.1101/2024.04.28.591464.

33. Gogos, J.A., Crabtree, G., and Diamantopoulou, A. (2020). The abiding relevance of mouse models of rare mutations to psychiatric neuroscience and therapeutics. Schizophr. Res. *217*, 37–51.

34. Diamantopoulou, A., and Gogos, J.A. (2019). Neurocognitive and Perceptual Processing in Genetic Mouse Models of Schizophrenia: Emerging Lessons. Neuroscientist *25*, 597–619.

35. Arguello, P.A., and Gogos, J.A. (2006). Modeling madness in mice: one piece at a time. Neuron *52*, 179–196.

36. Gordon, A., Forsingdal, A., Klewe, I.V., Nielsen, J., Didriksen, M., Werge, T., and Geschwind, D.H. (2019). Transcriptomic networks implicate neuronal energetic abnormalities in three mouse models harboring autism and schizophrenia-associated mutations. Molecular Psychiatry 2019 26:5 *26*, 1520–1534.

37. Siletti, K., Hodge, R., Mossi Albiach, A., Lee, K.W., Ding, S.-L., Hu, L., Lönnerberg, P., Bakken, T., Casper, T., Clark, M., et al. (2023). Transcriptomic diversity of cell types across the adult human brain. Science *382*, eadd7046.

38. Geschwind, D.H., and Flint, J. (2015). Genetics and genomics of psychiatric disease. Science *349*, 1489–1494.

39. Iossifov, I., O'Roak, B.J., Sanders, S.J., Ronemus, M., Krumm, N., Levy, D., Stessman, H.A., Witherspoon, K.T., Vives, L., Patterson, K.E., et al. (2014). The contribution of de novo coding mutations to autism spectrum disorder. Nature *515*, 216–221.

40. Matson, J.L., and Shoemaker, M. (2009). Intellectual disability and its relationship to autism spectrum disorders. Res. Dev. Disabil. *30*, 1107–1114.

41. Woodberry, K.A., Giuliano, A.J., and Seidman, L.J. (2008). Premorbid IQ in schizophrenia: a meta-analytic review. Am. J. Psychiatry *165*, 579–587.

42. Khandaker, G.M., Barnett, J.H., White, I.R., and Jones, P.B. (2011). A quantitative meta-analysis of population-based studies of premorbid intelligence and schizophrenia. Schizophr. Res. *132*, 220–227.

43. Creeth, H.D.J., Rees, E., Legge, S.E., Dennison, C.A., Holmans, P., Walters, J.T.R., O'Donovan, M.C., and Owen, M.J. (2022). Ultrarare coding variants and cognitive function in schizophrenia. JAMA Psychiatry *79*, 963–970.

44. Nuechterlein, K.H., Green, M.F., Kern, R.S., Baade, L.E., Barch, D.M., Cohen, J.D., Essock, S., Fenton, W.S., Frese, F.J., 3rd, Gold, J.M., et al. (2008). The MATRICS Consensus Cognitive Battery, part 1: test selection, reliability, and validity. Am. J. Psychiatry *165*, 203–213.

45. Mesholam-Gately, R.I., Giuliano, A.J., Goff, K.P., Faraone, S.V., and Seidman, L.J. (2009). Neurocognition in first-episode schizophrenia: a meta-analytic review. Neuropsychology *23*, 315–336.

46. Minshew, N.J., Goldstein, G., and Siegel, D.J. (1997). Neuropsychologic functioning in autism: profile of a complex information processing disorder. J. Int. Neuropsychol. Soc. *3*, 303–316.

47. Hill, E.L. (2004). Executive dysfunction in autism. Trends Cogn. Sci. *8*, 26–32.

48. Aleman, A., and Kahn, R. (2005). Strange feelings: Do amygdala abnormalities dysregulate the emotional brain in schizophrenia? Prog. Neurobiol. *77*, 283–298.

49. Baron-Cohen, S., Ring, H.A., Bullmore, E.T., Wheelwright, S., Ashwin, C., and Williams, S.C. (2000). The amygdala theory of autism. Neurosci. Biobehav. Rev. *24*, 355–364.

50. Banker, S.M., Gu, X., Schiller, D., and Foss-Feig, J.H. (2021). Hippocampal contributions to social and cognitive deficits in autism spectrum disorder. Trends Neurosci. *44*, 793–807.

51. Lieberman, J.A., Girgis, R.R., Brucato, G., Moore, H., Provenzano, F., Kegeles, L., Javitt, D., Kantrowitz, J., Wall, M.M., Corcoran, C.M., et al. (2018). Hippocampal dysfunction in the pathophysiology of schizophrenia: a selective review and hypothesis for early detection and intervention. Mol. Psychiatry *23*, 1764–1772.

52. Zierhut, K., Bogerts, B., Schott, B., Fenker, D., Walter, M., Albrecht, D., Steiner, J., Schütze, H., Northoff, G., Düzel, E., et al. (2010). The role of hippocampus dysfunction in deficient memory encoding and positive symptoms in schizophrenia. Psychiatry Res. *183*, 187–194.

53. Moberg, S., and Takahashi, N. (2022). Neocortical layer 5 subclasses: From cellular properties to roles in behavior. Front. Synaptic Neurosci. *14*, 1006773.

54. Jutla, A., Foss-Feig, J., and Veenstra-VanderWeele, J. (2022). Autism spectrum disorder and schizophrenia: An updated conceptual review. Autism Res. *15*, 384–412.

55. Palmer, D.S., Howrigan, D.P., Chapman, S.B., Adolfsson, R., Bass, N., Blackwood, D., Boks, M.P.M., Chen, C.-Y., Churchhouse, C., Corvin, A.P., et al. (2022). Exome sequencing in bipolar disorder identifies AKAP11 as a risk gene shared with schizophrenia. Nat. Genet. *54*, 541–547.

56. Kaplanis, J., Samocha, K.E., Wiel, L., Zhang, Z., Arvai, K.J., Eberhardt, R.Y., Gallone, G., Lelieveld, S.H., Martin, H.C., McRae, J.F., et al. (2020). Evidence for 28 genetic disorders discovered by combining healthcare and research data. Nature *586*, 757–762.

57. Karczewski, K.J., Francioli, L.C., Tiao, G., Cummings, B.B., Alföldi, J., Wang, Q., Collins, R.L., Laricchia, K.M., Ganna, A., Birnbaum, D.P., et al. (2020). The mutational constraint spectrum quantified from variation in 141,456 humans. Nature *581*, 434–443.

58. Chang, J., Gilman, S.R., Chiang, A.H., Sanders, S.J., and Vitkup, D. (2015). Genotype to phenotype relationships in autism spectrum disorders. Nat. Neurosci. *18*, 191–198.

59. Peça, J., Feliciano, C., Ting, J.T., Wang, W., Wells, M.F., Venkatraman, T.N., Lascola, C.D., Fu, Z., and Feng, G. (2011). Shank3 mutant mice display autistic-like behaviours and striatal dysfunction. Nature *472*, 437–442.

60. Rothwell, P.E., Fuccillo, M.V., Maxeiner, S., Hayton, S.J., Gokce, O., Lim, B.K., Fowler, S.C., Malenka, R.C., and Südhof, T.C. (2014). Autism-associated neuroligin-3 mutations commonly impair striatal circuits to boost repetitive behaviors. Cell *158*, 198–212.

61. Van Derveer, A.B., Bastos, G., Ferrell, A.D., Gallimore, C.G., Greene, M.L., Holmes, J.T., Kubricka, V., Ross, J.M., and Hamm, J.P. (2021). A role for somatostatin-positive interneurons in neuro-oscillatory and information processing deficits in schizophrenia. Schizophr. Bull. *47*, 1385–1398.

62. Batiuk, M.Y., Tyler, T., Dragicevic, K., Mei, S., Rydbirk, R., Petukhov, V., Deviatiiarov, R., Sedmak, D., Frank, E., Feher, V., et al. (2022). Upper cortical layer-driven network impairment in schizophrenia. Sci. Adv. *8*, eabn8367.

63. Chen, C.-Y., Tian, R., Ge, T., Lam, M., Sanchez-Andrade, G., Singh, T., Urpa, L., Liu, J.Z., Sanderson, M., Rowley, C., et al. (2023). The impact of rare protein coding genetic variation on adult cognitive function. Nat. Genet. *55*, 927–938.

64. Fawns-Ritchie, C., and Deary, I.J. (2020). Reliability and validity of the UK Biobank cognitive tests. PLoS One *15*, e0231627.

65. Marshall, C.R., Howrigan, D.P., Merico, D., Thiruvahindrapuram, B., Wu, W., Greer, D.S., Antaki, D., Shetty, A., Holmans, P.A., Pinto, D., et al. (2017). Contribution of copy number variants to schizophrenia from a genome-wide study of 41,321 subjects. Nat. Genet. *49*, 27–35.

66. Matsunami, N., Hadley, D., Hensel, C.H., Christensen, G.B., Kim, C., Frackelton, E., Thomas, K., da Silva, R.P., Stevens, J., Baird, L., et al. (2013). Identification of rare recurrent copy number variants in high-risk autism families and their prevalence in a large ASD population. PLoS One *8*, e52239.

67. Robin, N.H., and Shprintzen, R.J. (2005). Defining the clinical spectrum of deletion 22q11.2. J. Pediatr. *147*, 90–96.

68. Tang, K.L., Antshel, K.M., Fremont, W.P., and Kates, W.R. (2015). Behavioral and psychiatric phenotypes in 22q11.2 deletion syndrome. J. Dev. Behav. Pediatr. *36*, 639–650.

69. Swillen, A., Devriendt, K., Legius, E., Eyskens, B., Dumoulin, M., Gewillig, M., and Fryns, J.P. (1997). Intelligence and psychosocial adjustment in velocardiofacial syndrome: a study of 37 children and adolescents with VCFS. J. Med. Genet. *34*, 453–458.

70. Kepecs, A., and Fishell, G. (2014). Interneuron cell types are fit to function. Nature *505*, 318–326.

71. Chamberland, S., and Topolnik, L. (2012). Inhibitory control of hippocampal inhibitory neurons. Front. Neurosci. *0*, 165.

72. Letzkus, J.J., Wolff, S.B.E., and Lüthi, A. (2015). Disinhibition, a circuit mechanism for associative learning and memory. Neuron *88*, 264–276.

73. Pfeffer, C.K., Xue, M., He, M., Huang, Z.J., and Scanziani, M. (2013). Inhibition of inhibition in visual cortex: the logic of connections between molecularly distinct interneurons. Nat. Neurosci. *16*, 1068–1076.

74. Fu, Y., Tucciarone, J.M., Espinosa, J.S., Sheng, N., Darcy, D.P., Nicoll, R.A., and Stryker M (2014). A cortical circuit for gain control by behavioral state. Cell *156*, 1139–1152.

75. Bennett, C., Arroyo, S., Berns, D., and Hestrin, S. (2012). Mechanisms generating dual-component nicotinic EPSCs in cortical interneurons. J. Neurosci. *32*, 17287–17296.

76. Letzkus, J.J., Wolff, S.B.E., Meyer, E.M.M., Tovote, P., Courtin, J., Herry, C., and Lüthi, A. (2011). A disinhibitory microcircuit for associative fear learning in the auditory cortex. Nature *480*, 331–335.

77. Poorthuis, R.B., Enke, L., and Letzkus, J.J. (2014). Cholinergic circuit modulation through differential recruitment of neocortical interneuron types during behaviour: Cholinergic circuit modulation via interneurons. J. Physiol. *592*, 4155–4164.

78. Froemke, R.C., Merzenich, M.M., and Schreiner, C.E. (2007). A synaptic memory trace for cortical receptive field plasticity. Nature *450*, 425–429.

79. Lee, A.T., Cunniff, M.M., See, J.Z., Wilke, S.A., Luongo, F.J., Ellwood, I.T., Ponnavolu, S., and Sohal, V.S. (2019). VIP interneurons contribute to avoidance behavior by regulating information flow across hippocampal-prefrontal networks. Neuron *102*, 1223-1234.e4.

80. Stark, K.L., Xu, B., Bagchi, A., Lai, W.S., Liu, H., Hsu, R., Wan, X., Pavlidis, P., Mills, A.A., Karayiorgou, M., et al. (2008). Altered brain microRNA biogenesis contributes to phenotypic deficits in a 22q11-deletion mouse model. Nat. Genet. *40*, 751–760.

81. Drew, L.J., Stark, K.L., Fénelon, K., Karayiorgou, M., Macdermott, A.B., and Gogos, J.A. (2011). Evidence for altered hippocampal function in a mouse model of the human 22q11.2 microdeletion. Mol. Cell. Neurosci. *47*, 293–305.

82. Zaremba, J.D., Diamantopoulou, A., Danielson, N.B., Grosmark, A.D., Kaifosh, P.W., Bowler, J.C., Liao, Z., Sparks, F.T., Gogos, J.A., and Losonczy, A. (2017). Impaired hippocampal place cell dynamics in a mouse model of the 22q11.2 deletion. Nat. Neurosci. *20*, 1612–1623.

83. Sun, Z., Williams, D.J., Xu, B., and Gogos, J.A. (2018). Altered function and maturation of primary cortical neurons from a 22q11.2 deletion mouse model of schizophrenia. Transl. Psychiatry *8*. https://doi.org/10.1038/s41398-018-0132-8.

84. Geiller, T., Vancura, B., Terada, S., Troullinou, E., Chavlis, S., Tsagkatakis, G., Tsakalides, P., Ócsai, K., Poirazi, P., Rózsa, B.J., et al. (2020). Large-Scale 3D Two-Photon Imaging of Molecularly Identified CA1 Interneuron Dynamics in Behaving Mice. Neuron *108*, 968-983.e9.

85. Szalay, G., Judák, L., Katona, G., Ócsai, K., Juhász, G., Veress, M., Szadai, Z., Fehér, A., Tompa, T., Chiovini, B., et al. (2016). Fast 3D imaging of spine, dendritic, and neuronal assemblies in behaving animals. Neuron *92*, 723–738.

86. Katona, G., Szalay, G., Maák, P., Kaszás, A., Veress, M., Hillier, D., Chiovini, B., Vizi, E.S., Roska, B., and Rózsa, B. (2012). Fast two-photon in vivo imaging with three-dimensional random-access scanning in large tissue volumes. Nat. Methods *9*, 201–208.

87. Vancura, B., Geiller, T., Grosmark, A., Zhao, V., and Losonczy, A. (2023). Inhibitory control of sharp-wave ripple duration during learning in hippocampal recurrent networks. Nat. Neurosci. *26*, 788–797.

88. Somogyi, P., and Klausberger, T. (2005). Defined types of cortical interneurone structure space and spike timing in the hippocampus. J. Physiol. *562*, 9–26.

89. Guet-McCreight, A., Skinner, F.K., and Topolnik, L. (2020). Common principles in functional organization of VIP/calretinin cell-driven disinhibitory circuits across cortical areas. Front. Neural Circuits *14*, 32.

90. Varga, C., Golshani, P., and Soltesz, I. (2012). Frequency-invariant temporal ordering of interneuronal discharges during hippocampal oscillations in awake mice. Proc. Natl. Acad. Sci. U. S. A. *109*, E2726-34.

91. Lapray, D., Lasztoczi, B., Lagler, M., Viney, T.J., Katona, L., Valenti, O., Hartwich, K., Borhegyi, Z., Somogyi, P., and Klausberger, T. (2012). Behavior-dependent specialization of identified hippocampal interneurons. Nat. Neurosci. *15*, 1265–1271.

92. Katona, L., Lapray, D., Viney, T.J., Oulhaj, A., Borhegyi, Z., Micklem, B.R., Klausberger, T., and Somogyi, P. (2014). Sleep and movement differentiates actions of two types of somatostatin-expressing GABAergic interneuron in rat hippocampus. Neuron *82*, 872–886.

93. Somogyi, P., Katona, L., Klausberger, T., Lasztóczi, B., and Viney, T.J. (2014). Temporal redistribution of inhibition over neuronal subcellular domains underlies state-dependent rhythmic change of excitability in the hippocampus. Philos. Trans. R. Soc. Lond. B Biol. Sci. *369*, 20120518.

94. Turi, G.F., Li, W.-K., Chavlis, S., Pandi, I., Hare, J.O., Priestley, J.B., Grosmark, A.D., Liao, Z., Ladow, M., Zhang, J.F., et al. (2019). Vasoactive Intestinal Polypeptide-Expressing Interneurons in the Hippocampus Support Goal-Oriented Spatial Learning. Neuron, 1–16.

95. Dudok, B., Klein, P.M., Hwaun, E., Lee, B.R., Yao, Z., Fong, O., Bowler, J.C., Terada, S., Sparks, F.T., Szabo, G.G., et al. (2021). Alternating sources of perisomatic inhibition during behavior. Neuron *109*, 997-1012.e9.

96. Friedrich, J., Zhou, P., and Paninski, L. (2017). Fast online deconvolution of calcium imaging data. PLoS Comput. Biol. *13*, e1005423.

97. Buzsáki, G., and Moser, E.I. (2013). Memory, navigation and theta rhythm in the hippocampal-entorhinal system. Nature Neuroscience 2013 16:2 *16*, 130–138.

98. O'Keefe, J., and Dostrovsky, J. (1971). The hippocampus as a spatial map. Preliminary evidence from unit activity in the freely-moving rat. Brain Res. *34*, 171–175.

99. Robinson, E.B., Samocha, K.E., Kosmicki, J.A., McGrath, L., Neale, B.M., Perlis, R.H., and Daly, M.J. (2014). Autism spectrum disorder severity reflects the average contribution of de novo and familial influences. Proc. Natl. Acad. Sci. U. S. A. *111*, 15161–15165.

100. Gonzalez-Burgos, G., and Lewis, D.A. (2012). NMDA receptor hypofunction, parvalbumin-positive neurons, and cortical gamma oscillations in schizophrenia. Schizophr. Bull. *38*, 950–957.

101. Buzsáki, G., and Draguhn, A. (2004). Neuronal oscillations in cortical networks. Science *304*, 1926–1929.

102. Möhler, H., and Rudolph, U. (2017). Disinhibition, an emerging pharmacology of learning and memory. F1000Res. *6*, 101.

103. Lovett-Barron, M., and Losonczy, A. (2014). Behavioral consequences of GABAergic neuronal diversity. Curr. Opin. Neurobiol. *26*, 27–33.

104. Luo, X., Guet-McCreight, A., Villette, V., Francavilla, R., Marino, B., Chamberland, S., Skinner, F.K., and Topolnik, L. (2020). Synaptic mechanisms underlying the network state-dependent recruitment of VIP-expressing interneurons in the CA1 hippocampus. Cereb. Cortex *30*, 3667–3685.

105. Kamigaki, T., and Dan, Y. (2017). Delay activity of specific prefrontal interneuron subtypes modulates memory-guided behavior. Nat. Neurosci. *20*, 854–863.

106. Goff, K.M., and Goldberg, E.M. (2021). A role for vasoactive intestinal peptide interneurons in neurodevelopmental disorders. Dev. Neurosci. *43*, 168–180.

107. Mossner, J.M., Batista-Brito, R., Pant, R., and Cardin, J.A. (2020). Developmental loss of MeCP2 from VIP interneurons impairs cortical function and behavior. Elife *9*. https://doi.org/10.7554/eLife.55639.

108. Goff, K.M., Liebergall, S.R., Jiang, E., Somarowthu, A., and Goldberg, E.M. (2023). VIP interneuron impairment promotes in vivo circuit dysfunction and autism-related behaviors in Dravet syndrome. Cell Rep. *42*, 112628.

109. Murray, J.D., Anticevic, A., Gancsos, M., Ichinose, M., Corlett, P.R., Krystal, J.H., and Wang, X.-J. (2014). Linking microcircuit dysfunction to cognitive impairment: effects of disinhibition associated with schizophrenia in a cortical working memory model. Cereb. Cortex *24*, 859–872.

110. Ioannidis, N.M., Rothstein, J.H., Pejaver, V., Middha, S., McDonnell, S.K., Baheti, S., Musolf, A., Li, Q., Holzinger, E., Karyadi, D., et al. (2016). REVEL: An Ensemble Method for Predicting the Pathogenicity of Rare Missense Variants. Am. J. Hum. Genet. *99*, 877–885.

111. Samocha, K.E., Kosmicki, J.A., Karczewski, K.J., O'Donnell-Luria, A.H., Pierce-Hoffman, E., MacArthur, D.G., Neale, B.M., and Daly, M.J. (2017). Regional missense constraint improves variant deleteriousness prediction. bioRxiv, 148353. https://doi.org/10.1101/148353.

112. Kang, H.J., Kawasawa, Y.I., Cheng, F., Zhu, Y., Xu, X., Li, M., Sousa, A.M.M., Pletikos, M., Meyer, K.A., Sedmak, G., et al. (2011). Spatio-temporal transcriptome of the human brain. Nature *478*, 483–489.

113. Lovett-Barron, M., Kaifosh, P., Kheirbek, M.A., Danielson, N., Zaremba, J.D., Reardon, T.R., Turi, G.F., Hen, R., Zemelman, B.V., and Losonczy, A. (2014). Dendritic inhibition in the hippocampus supports fear learning. Science *343*, 857–863.

114. Acsády, L., Görcs, T.J., and Freund, T.F. (1996). Different populations of vasoactive intestinal polypeptide-immunoreactive interneurons are specialized to control pyramidal cells or interneurons in the hippocampus. Neuroscience *73*, 317–334.

115. Acsády, L., Arabadzisz, D., and Freund, T.F. (1996). Correlated morphological and neurochemical features identify different subsets of vasoactive intestinal polypeptide-immunoreactive interneurons in rat hippocampus. Neuroscience *73*, 299–315.

116. Tyan, L., Chamberland, S., Magnin, E., Camiré, O., Francavilla, R., David, L.S., Deisseroth, K., and Topolnik, L. (2014). Dendritic inhibition provided by interneuron-specific cells controls the firing rate and timing of the hippocampal feedback inhibitory circuitry. J. Neurosci. *34*, 4534–4547.

117. Pelkey, K.A., Chittajallu, R., Craig, M.T., Tricoire, L., Wester, J.C., and Mcbain, X.C.J. (2017). Hippocampal GABAergic inhibitory interneurons. Physiol. Rev. *97*, 1619–1747.

118. Francavilla, R., Villette, V., Luo, X., Chamberland, S., Muñoz-Pino, E., Camiré, O., Wagner, K., Kis, V., Somogyi, P., and Topolnik, L. (2018). Connectivity and network state-dependent recruitment of long-range VIP-GABAergic neurons in the mouse hippocampus. Nat. Commun. *9*, 5043.

119. Kaifosh, P., Zaremba, J.D., Danielson, N.B., and Losonczy, A. (2014). SIMA: Python software for analysis of dynamic fluorescence imaging data. Front. Neuroinform. *8*, 80.

120. Satterstrom, F.K., Kosmicki, J.A., Wang, J., Breen, M.S., De Rubeis, S., An, J.-Y., Peng, M., Collins, R., Grove, J., Klei, L., et al. (2020). Large-Scale Exome Sequencing Study Implicates Both Developmental and Functional Changes in the Neurobiology of Autism. Cell *180*, 568-584.e23.